POLITECNICO DI MILANO
Scuola di Ingegneria Industriale e dell'Informazione
Master Degree in Engineering Physics

SUSPENDED GRAPHENE ON GE MICRO-CRYSTALS

Supervisor: Prof.Giovanni Isella
Co-supervisor: Dr.Andrea Ballabio

Master thesis by:
Virginia Falcone
898872

Academic Year 2018-2019

Abstract

Ge micro-crystals can be grown by means of a Low-Energy Plasma-Enhanced CVD (LEPECVD) tool, exploiting the "self-assembling" growth of Ge/Si crystals on a patterned Si substrate. This vertical epitaxy, able to produce 3D micro-crystals, several micrometer tall, is characterized by a limited lateral expansion of the epitaxial micro-crystals and, by optimizing the growth parameters, it is possible to achieve a complete expulsion of threading dislocations and an high light confinement with an elevated surface fill factor. Therefore, Ge micro-crystals are appealing as building blocks for optoelectronic devices, able to operate in the near-infrared spectral region.

In this thesis the optimization of different fabrication steps of these devices is presented, in particular the formation of a top transparent contact by using graphene. In fact the absorption of a graphene monolayer does not exceed 2.4% and so, using it as a contact, allows to reduce the absorption when compared to a metal contact. The fabricated devices are characterized by means of electrical and optical measurements, and in particular the photocurrent and the photoresponse measurements confirm the capability to fabricate optoelectronic devices made by Ge micro-crystals, exploiting the graphene properties as a non conventional electrical contact.

Contents

Chapter 1 .... **1**
Graphene/Semiconductor heterojunctions **1**
1.1 Introduction 1
1.2 Metal/semiconductor junction 2
1.2.1 Forward and Reverse bias 6
1.3 Graphene 8
1.3.1 Conduction properties 8
1.3.2 Optical properties 11
1.4 Graphene/Semiconductor junction 11

Chapter 2 .... **15**
3D heteroepitaxy and fabrication process **15**
2.1 Introduction 15
2.2 Vertical epitaxial growth of micro-crystals 16
2.3 Device Structure 18
2.4 Fabrication Process 20
2.4.1 Graphene Transfer 25
2.4.2 Optimization of the Graphene contact 28
2.4.2.1 SOG (spin-on-glass) oxide 28
2.4.2.2 Optimization of the PMMA removal 28
2.4.2.3 Increasing graphene resistance 31

Chapter 3 .... **36**
Electro-optical characterization **36**
3.1 Experimental setup 36
3.2 Photocurrent measurements 40
3.3 Estimation of the energy gap 45

3.4 Conclusion and future work 50

Appendix A 53

1. Optical lithography 53

Appendix B 55

1. Cryogenic deep RIE 55
2. Electron-beam evaporation 56
3. Plasma asher and rapid thermal annealing (RTA) 57

Bibliography 59

List of Figures

Figure 1.1: Structure of the final device.. 2
Figure 1.2: Energy band alignments of a metal and a n-type semiconductor before the contact... 5
Figure 1.3: Creation of the depletion layer in the n-type semiconductor.. 5
Figure 1.4: Schottky junction between a metal and a n-type semiconductor.. 6
Figure 1.5: I-V of a rectifying Schottky junction.................................. 7
Figure 1.6: Hexagonal lattice of the graphene, where $\overrightarrow{a_1}$ and $\overrightarrow{a_2}$ are the primitive lattice vectors.. 9
Figure 1.7: Band Structure of the graphene with the two sets of inequivalent points...10
Figure 1.8: Energy band diagram of the graphene-semiconductor Schottky junction.. 12
Figure 1.9: Graphene-semiconductor junction with reverse bias applied and electron-hole pair generation in the depletion layer..... 13
Figure 2.1: LEPECVD growth process, where the bonds are broken by the plasma leading to the deposition of reactive species.................... 17
Figure 2.2: Scheme of the LG2 reactor 17
Figure 2.3: SEM cross section image of 10 µm of Ge on a patterned Si substrate.. 18
Figure 2.4: On the left the structure of i-Ge micro-crystals. On the right a representation of the band diagram at the interface between n-Si and i-Ge.. 19
Figure 2.5: SEM images of the pattern A after growth........................20

Figure 2.6: (a) Growth sample; (b) deposition of SiO_2; (c) removal of the silicon dioxide in the patterned region; (d) generation of the metallic pad; (e) graphene transfer; (f) final device structure............ 22
Figure 2.7: Mask used for the first optical lithography step.............. 23
Figure 2.8: SEM image of the metallic pad of Au/Al/Ti on SiO_2....... 24
Figure 2.9: SEM image represented the metallic pad and the micro-crystals pattern... 24
Figure 2.10: Representation of the different steps of the graphene transfer 26
Figure 2.11: (a) Graphene with PMMA on the pattern region; (b) Graphene after the removal of the PMMA.. 27
Figure 2.12: SEM image of the pattern post filling with SOG............ 29
Figure 2.13: (a) Graphene on Ge micro-crystals after the PMMA removal with the vacuum oven; (b) Graphene on Ge micro-crystals after the PMMA removal in the RTA with the Ar and H_2 flux.......... 30
Figure 2.14: Graphene on Ge micro-crystals after the PMMA removal in the RTA with the N_2 flux.. 31
Figure 2.15: Graphene with 7 nm of Au after the removal of PMMA 32
Figure 2.16: Bilayer of graphene on Pattern A with magnification 5000x.. 33
Figure 2.17: Bilayer of graphene on the pattern D, on the right SEM image with a magnification of 3740x while on the left image with a magnification of 748x... 34
Figure 3.1: Representation of the experimental setup used for the electro-optical measurements.. 37
Figure 3.2: (a) Image of the sample on a Copper plate used for the back contact connection; (b) Probe used to land on the metallic pad for the electrical measurements. 38

Figure 3.3: SEM images of the patterns used for the measurements: (a)pattern A; (b) pattern B; (c) pattern C; (d) pattern D; (e) pattern F 39
Figure 3.4: I-V characteristics for pattern A, J, D and F...................... 40
Figure 3.5: Photocurrent measurement of pattern A, D and C.......... 41
Figure 3.6: SEM image represented the PMMA impurity in the graphene layer of the pattern C 42
Figure 3.7: Measure of photocurrent of the pattern B and of the unpatterned area close to the pattern B 43
Figure 3.8: Responsivity obtained with a confocal microscope.......... 44
Figure 3.9: Normalized Photocurrent of patterns A, B and D............ 44
Figure 3.10: Vertical transition from the valence band to the conduction one.. 46
Figure 3.11: Proof of the validity of the approximation...................... 49
Figure 3.12: Estimate of the energy gap for the pattern F 49
Figure 3.13: Estimate of the energy gap for the pattern D 50
Figure 3.14: The structure of the optimal Ge micro-crystals made by top p-Ge/i-Ge/n++ Si 51
Figure A.1: Sketch of the optical lithography process 54
Figure B.1: RIE machine sketch 56

List of Tables

Table 2.1:Patterns characteristic dimensions…………………………19

Chapter 1

Graphene/Semiconductor heterojunctions

1.1 Introduction

The investigation of the optoelectronic properties of Ge micro-crystals, for their use in photodetectors in the near-infrared region, has led to the problem of achieving a transparent contact on these 3D structures. In this thesis the optimization of the different steps required to fabricate the device shown in Figure 1.1 are presented, in particular the analysis of the top contact formation using graphene. Indeed thanks to its two dimensional nature and its physical properties, graphene seems to be the optimal choice for the fabrication of the targeted device. In fact graphene allows to obtain a top transparent contact given its absorption of 2.4% of the incoming photon for each monolayer and guarantees the formation of a continuous contact despite the gap between the pillars. The experimental aspects related to the fabrication of a suspended

graphene layer on top of Ge micro-crystals will be described in the next chapter, here we will focus on the electronic aspects related to the formation of a graphene/semiconductor contact.

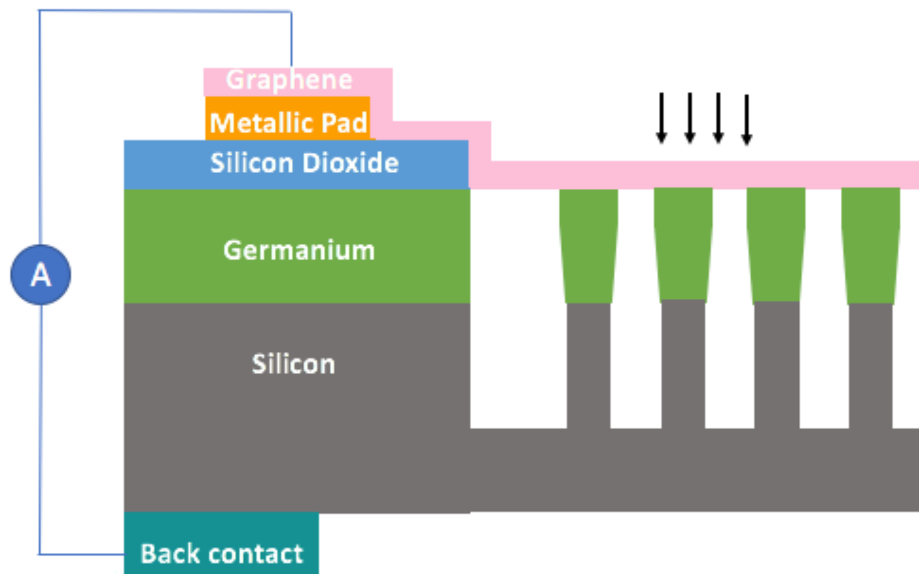

Figure 1.1: Structure of the final device.

1.2 Metal/semiconductor junction

Graphene is a zero-gap semiconductor, however a non-intentional doping can arise from the coupling of graphene with the surface of another material, or due to the treatments that must be done to manipulate it. Due to non-intentional doping graphene should have a non-zero population of carrier in the conduction or valence band depending on the doping. Usually a wet transfer process, like that used in this thesis, leads to a p-type behavior. For this reason, graphene can, as a first approximation, be considered a metal and therefore, with the aim of studying the graphene/semiconductor

junction, it is worth to analyze a more common and well studied junction which is the metal/semiconductor one.

The contact between a metal and a semiconductor can lead to the formation of two types of junctions: Ohmic and Schottky (also called rectifying junction). A Schottky junction is formed when the semiconductor has a lower work function than the metal, while when the semiconductor has a higher work function the junction formed is Ohmic. In case of an Ohmic junction, after the contact between the metal and the semiconductor, electrons move from the metal to the conduction band of the semiconductor implying the generation of an accumulation region. In this way this type of junction behaves as a resistor conducting symmetrically both under forward and reverse bias. The current varies linearly with the applied voltage and depends also on the total resistance that is given by the sum between the contact (R_c) and the series resistance (R_s).

$$\frac{V}{I} = R_c + R_s \tag{1.0}$$

The second type of junction is the Schottky one, for the sake of clarity and brevity, a junction between metal and n-type semiconductor will be considered. As shown in Figure 1.2, before their contact, considering an equal vacuum level for the metal and the semiconductor, it is possible to see that the work function of the metal itself is greater than that of the semiconductor, since the Fermi level of the semiconductor is closer to the vacuum level than the metal Fermi level. When the metal-semiconductor junction is formed the Fermi levels must line up at equilibrium, so electrons in the conduction band of the semiconductor move to the empty states of the metal. The removal of electrons generates a region of positive

charge called depletion layer that consists of uncompensated dopant ions, as shown in Figure 1.3. As a consequence a thin layer of charges of opposite sign, will be at the metal-semiconductor interface, implying the generation of an electric field E_0 and a built in potential V_0. The energy bands bend up in the direction of the electric field so going from the n-type semiconductor to the metal, and this bending is extended in the depletion layer itself, as can be seen in Figure 1.4. The energy difference between the conduction band at the interface and in the bulk, is related to the built-in potential, and represent the height of the barrier for the electrons that are moving from the semiconductor to the metal. The built-in potential eV_0 is given by:

$$eV_0 = \phi_m - \phi_n \tag{1.1}$$

where ϕ_m is the work function of the metal and ϕ_n is the work function of the semiconductor. The height of the energy barrier for electrons moving from the metal to the semiconductor, the Schottky barrier height (SBH), is:

$$\phi_{SBH} = \phi_m - \chi_n \tag{1.2}$$

where χ_n is the electron affinity of the n-type semiconductor. It is relevant to note that the SBH (Eq. 1.2) depends only on physical parameters of the materials involved, while the barrier seen by the electrons (Eq. 1.1) can be tuned with external factors, such as the applied electric field or the semiconductor doping.

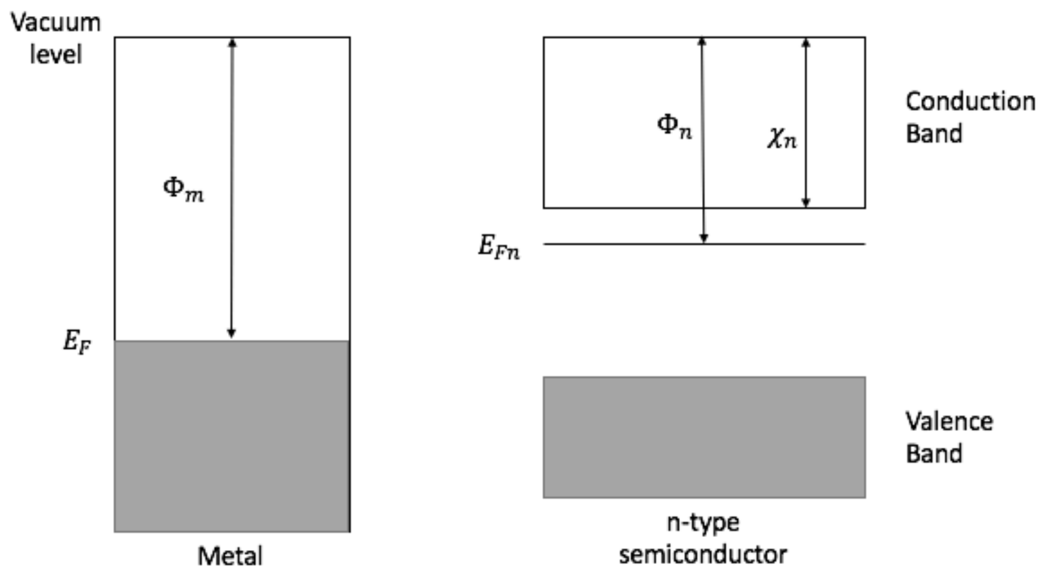

Figure 1.2: Energy band alignments of a metal and a n-type semiconductor before the contact.

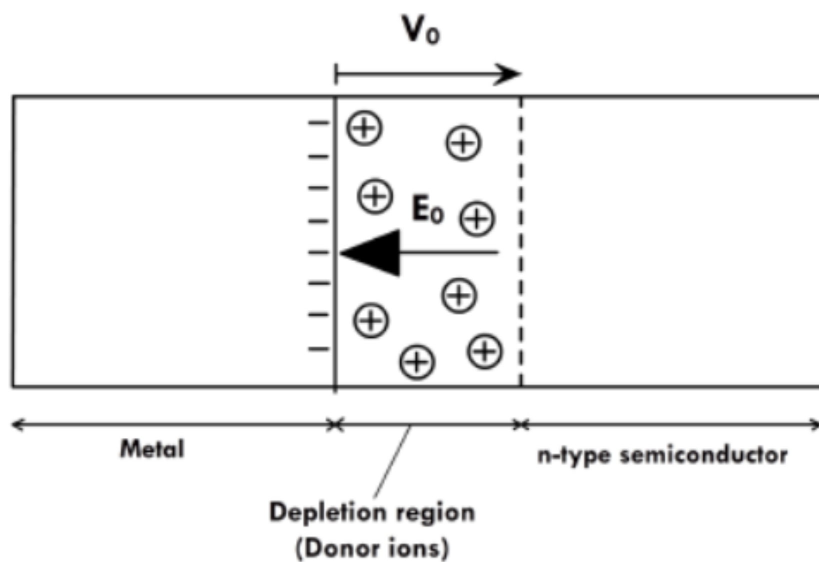

Figure 1.3: Creation of the depletion layer in the n-type semiconductor, taken from ref. [1] page 478.

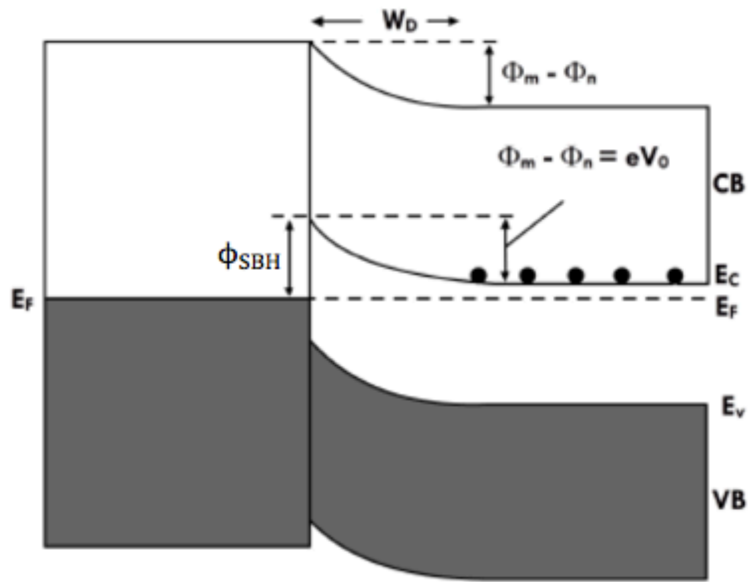

Figure 1.4: Schottky junction between a metal and a n-type semiconductor. In the semiconductor it is possible to see the band bending close to the interface, taken from ref. [1] page 478.

1.2.1 Forward and Reverse bias

As already mentioned, the application of an external bias can play an important role on the Schottky junction. By the application of a bias the Fermi level of the metal and of the semiconductor are no more aligned but are shifted by an amount equal to the applied voltage. First of all, we can distinguish two types of bias: forward bias, when the metal is connected to the positive terminal and the semiconductor to the negative one, and the opposite condition so called reverse bias. In forward bias the external potential is applied such that it opposes the built-in potential of the Schottky junction. In this condition the electrons going from the semiconductor to the metal see a lower barrier and, as a consequence, there is an increase of the current by increasing the forward bias.

The density of current J for an applied voltage V is given by:

$$J = J_0 \left[exp\left(\frac{eV}{k_B T}\right) - 1\right] \qquad (1.3)$$

Where J_0 depends on the Schottky barrier and is defined as:

$$J_0 = A^* T^2 exp\left(\frac{-\phi_{SBH}}{k_B T}\right) \qquad (1.4)$$

where A^* is the effective Richardson constant, T the temperature expressed in Kelvin and k_B the Boltzmann constant. Instead in reverse bias, the voltage is applied in the same direction of the built-in potential, so now the electrons are moving from the metal to the semiconductor.
These electrons see the Schottky barrier (SBH) that is independent on the bias applied and so in this regime there is always a constant current equal to J_0. In conclusion, the Schottky junction has a rectifying behavior with an exponential increase of the current in forward bias and a small constant current in reverse bias (Figure 1.5).

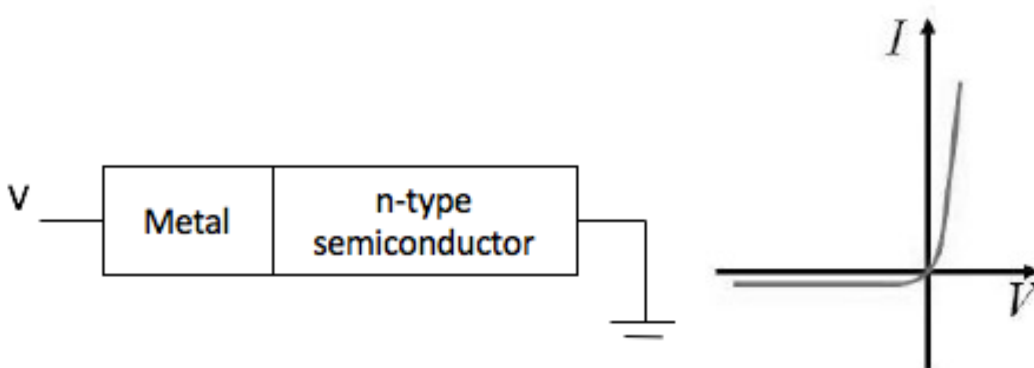

Figure 1.5: I-V of a rectifying Schottky junction, taken from ref [2].

1.3 Graphene

Graphene is a one-atom-thick layer of carbon atoms arranged in a hexagonal lattice, that can be seen as two interpenetrating triangular sub-lattices A and B (Figure 1.6). Each atom of carbon is covalently bond with three other atoms, while the remaining p_z electron per atom gives rise to delocalized states.

1.3.1 Conduction properties

Graphene is a zero-gap semiconductor because the conduction band and the valence band touch each other in the reciprocal space in 6 points, that can be separated in two non-equivalent set $\vec{K}$ and $\vec{K'}$ called Dirac points, as shown in Figure 1.7.

Close to the Dirac points the dispersion relation is linear, so carriers in graphene behaves as relativistic particles that moves at constant speed equal to v_F, and the electron equation is equivalent to a 2D Dirac equation for massless fermions.

It's also important to consider that due to the two interpenetrating sub-lattices, electrons near the Dirac point can be described by a two component wavefunction (ref. [4]):

$$\psi_{\pm,\vec{K}}(\vec{k}) = \frac{1}{\sqrt{2}} \begin{pmatrix} e^{-i\theta_k/2} \\ \pm e^{i\theta_k/2} \end{pmatrix} \tag{1.4}$$

where $\theta_k = arctan\left(\frac{q_x}{q_y}\right)$ and $\vec{q} = \vec{k} - \vec{K}$ is the momentum from the $\vec{K}$ Dirac point.

This implies that electrons with $+k_x$ and $-k_x$ have orthogonal wavefunction, so it is not possible to have a backscattering event of 180°, this leads to an extremely high carrier mobility. The mobility can be defined in a ballistic regime as:

$$\mu = \frac{\sigma}{en} \tag{1.5}$$

In this regime the mobility of graphene can reach values of the order of $2 \times 10^5\ cm^2\ V^{-1}s^{-1}$ for $n < 5{\times}10^9 cm^{-2}$ (ref. [5] and [6]) and the conductivity is proportional to the square root of the carrier density n. Instead when the scattering events are predominant, transport is diffusive and a reduction in mobility can be measured ($10^3\ cm^2\ V^{-1}s^{-1}$ ref. [7]).

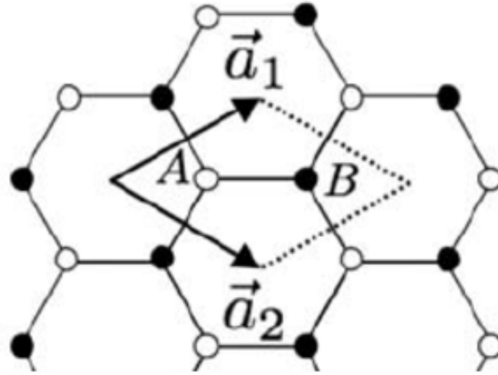

Figure 1.6: Hexagonal lattice of graphene, where $\overrightarrow{a_1}$ and $\overrightarrow{a_2}$ are the primitive lattice vectors, taken from ref [3].

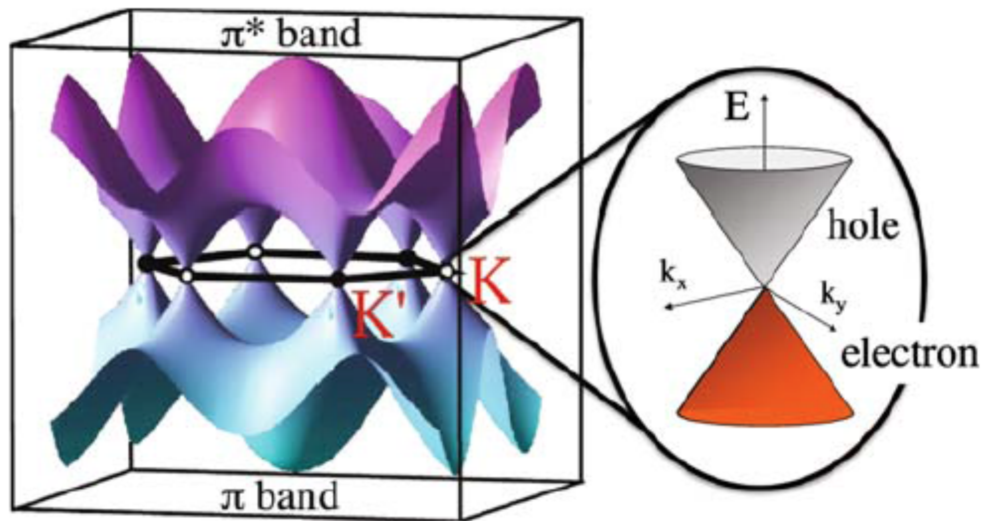

Figure 1.7: Band structure of graphene with the two sets of inequivalent Dirac points, taken from ref [3].

In graphene we can distinguish three main types of scattering mechanisms that influence the final conductivity in the diffusive regime:

1. Coulomb scattering by charged impurities;
2. Electron-phonon scattering;
3. Short-range scattering;

For each of these mechanisms it is possible to define a conductivity σ_i such that the total conductivity will be given by:

$$\frac{1}{\sigma_{Tot}} = \frac{1}{\sigma_1} + \frac{1}{\sigma_2} + \cdots \qquad (1.6)$$

1.3.2 Optical properties

Graphene stands out not only for its conduction properties but also for its optical properties. Indeed it is characterized by a transmittance that is independent on the wavelength and, in case of normal incidence, the absorption is $A = 1 - T \sim 2.4\%$ (ref.[8]).
Considering that a single layer of graphene has a thickness of 0.334 nm, this is a considerable absorption. Despite this, the advantage of using graphene is that usually to contact the device we need just one single layer so the absorption remains low with respect to the absorption given by a metal contact of suitable thickness. If the number of graphene layers is duplicated, its absorption is also duplicated but nevertheless transparency remains high.

1.4 Graphene/Semiconductor junction

In the literature it has been proved that the ideal graphene-semiconductor junction (GSJ) is a Schottky junction ref. [9,10,11], as can be represented in Figure 1.8. Therefore, the current-voltage (I-V) behavior can be described by the ideal diode equation (Eq. 1.3). The advantage of using graphene is that its Fermi level is extremely sensitive to the number of carriers injected from or into the semiconductor, by the applied bias:

$$E_F = \mp \frac{h}{2\sqrt{\pi}} v_F \sqrt{n} \quad (1.7)$$

Thanks to this dependence of the Fermi level on *n*, we can control, by the application of a bias, the Fermi energy, the sign of the excess carriers and the conductivity of the graphene layer. Moreover the Fermi level influences also the Schottky junction behavior, implying a variation in the current-voltage characteristic of the junction.
The optical properties of graphene and its high carrier mobility make the graphene-semiconductor junction an ideal photodetector. Indeed graphene allows almost 98% of the light to pass through into the semiconductor, where electron-hole pairs are generated (see Figure 1.9).

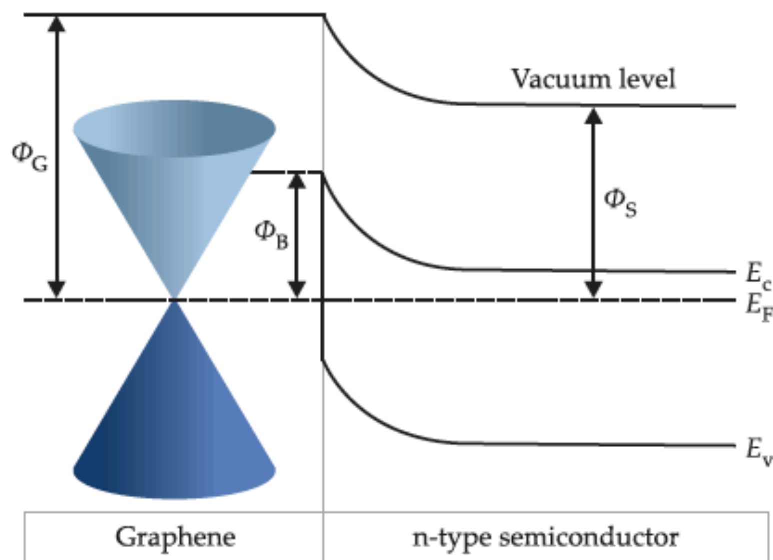

Figure 1.8: Energy band diagram of the graphene-semiconductor Schottky junction, taken from ref [9].

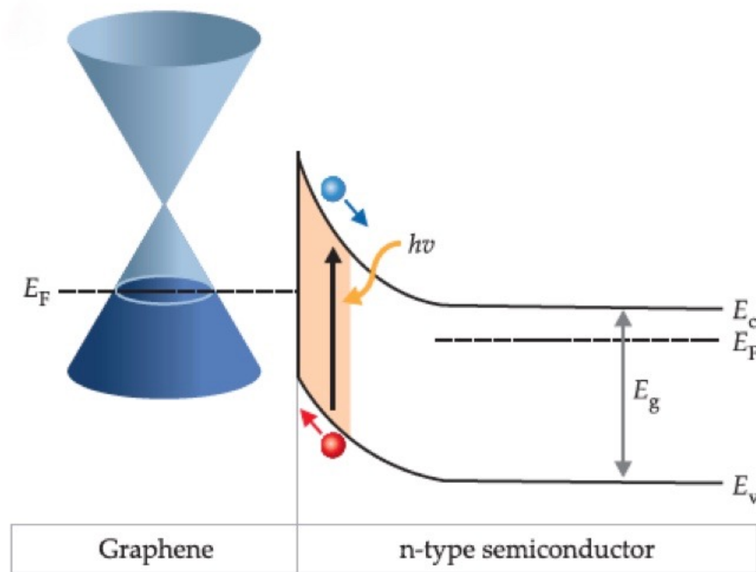

Figure 1.9: Graphene-semiconductor junction with reverse bias applied and electron-hole pair generation in the depletion layer, taken from ref [9].

Several experimental results have already been obtained to exploit this property of the graphene-semiconductor junction (ref.[12,13]). In ref.[12] selectively fully coherent germanium (Ge) islands on nanotip patterned Si(001) substrates have been grown and the formation of a single-layer graphene/Ge/Si-tip Schottky junctions to be used as photodetection has been proven. In ref. [13] 1 μm tall and a few hundred of nm wide Ge nanopillars have been obtained by etching a Ge epilayer. Also in this case a suspended graphene layer has been used as a transparent top-contact.
In both approaches the active volume is extremely limited due to the nanometric dimension of the Ge structures. By using Ge micro-crystals we can leverage on the higher volume and fill factor featured by such microstructures to improve the photodetector performances.

Chapter 2

3D heteroepitaxy and fabrication process

2.1 Introduction

The thesis work is focused on the realization of photodetectors operating in the near-infrared, using Ge micro-crystals as the absorbing medium. The choice of a suitable top transparent contact for these non-planar structures can be graphene because, as we have seen in chapter 1, graphene has excellent conductance and optical properties and a Schottky junction is produced at the graphene/semiconductor interface. Nonetheless, the fabrication process is a critical aspect in the realization of the final device due to the 3D morphology of Ge micro-crystals and the presence of a 100-500 nm gap separating the micro-crystals which need to be bridged by the graphene layer. In this chapter, after a brief description of the method used for the epitaxial growth of Ge micro-crystals, I will describe the fabrication method developed during my

thesis for the formation of a graphene layer suspended on the micro-crystals array.

2.2 Vertical epitaxial growth of micro-crystals

The micro-crystals of Ge are obtained by low-energy plasma-enhanced chemical vapor deposition (LEPECVD). This growth technique is similar to the standard CVD process but for a plasma which is generated in the chamber to enhance the deposition rate. The sample is placed in an ultra-high vacuum (UHV) chamber and it is heated up to the growth temperature. Then an argon plasma is produced in the chamber, and the precursor gases, SiH_4 for silicon deposition or GeH_4 for germanium, are introduced. The plasma excites the precursor gases, and the reactive species are then adsorbed on the surface of the substrate while the remaining part is pumped away (Figure 2.1). Thanks to the high reactive conditions implied by the plasma, the material is deposited quickly on the substrate, and the growth rates can be controlled by varying the plasma density and the amount of process gas. The LEPECVD tool in which the samples for this thesis are grown is called LG2 (LEPECVD generation 2) and a scheme of this machine is represented in Figure 2.2. The UHV chamber is maintained at a pressure of 10^{-8} mbar by a turbomolecular and a rough pump, a loadlock chamber is used to introduce the wafers in the chamber, in order not to brake the UHV in the main chamber. The wafer is kept, facing down, at a floating potential, right above the plasma source, where the argon gas flux is ionized by electrons thermionically emitted by a tantalum filament.

The plasma is then ignited by a DC arc discharge from the heated filaments to the grounded chamber walls. The confinement of the plasma is guaranteed by an anode ring and a magnetic field induced by copper coils.

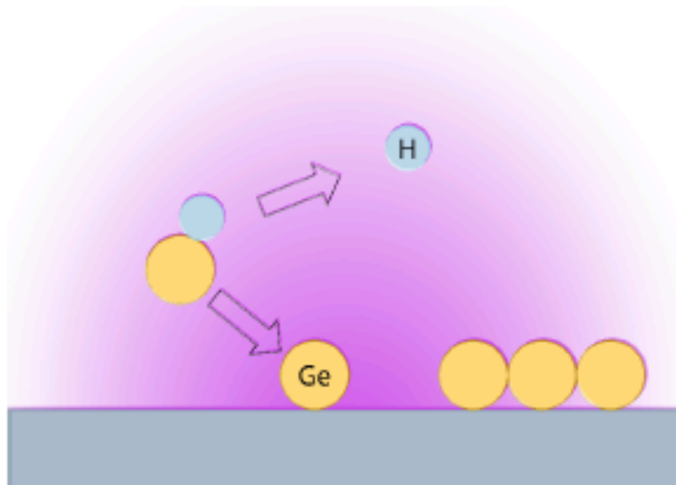

Figure 2.1: LEPECVD growth process, where the bonds are broken by the plasma leading to the deposition of the reactive species.

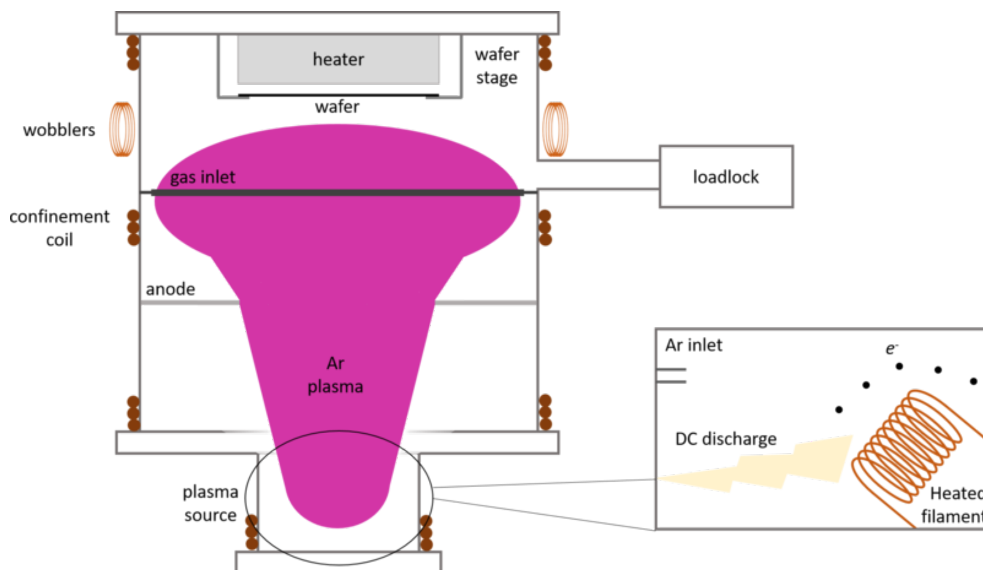

Figure 2.2: Scheme of the LG2 reactor.

It has been proven in ref.[14] how the vertical growth of Ge micro-crystals with high aspects ratio can be implemented by deposition on a patterned substrate (Figure 2.3). This is an effect related to the particular growth parameters achievable in a LEPECVD reactor which lead to high deposition rate (approx. 5 nm/s) and relatively low temperatures (typically 500°C). Indeed, the final shape of the Ge micro-crystals is determined by the relative growth speed of the different facets of the crystal itself and so the final shape is defined by the minimization of the total growth rate of the crystal.

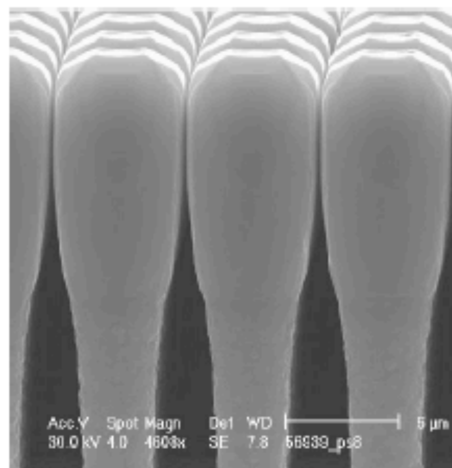

Figure 2.3: SEM cross section image of 10 µm of Ge on a patterned Si substrate.

2.3 Device Structure

The self-assembling of Ge crystals is driven by a patterned Si substrate. The Si patterning is obtained by means of optical lithography (see Appendix A) and cryogenic deep RIE etching (see Appendix B.1), of a silicon wafer. The sample used for device fabrication consists of microcrystals of intrinsic Ge, 8 µm high, deposited on n++ Si micro-pillars. The use of a n-Si substrate implies a small conduction band offset between i-Ge and n-Si. In this way

electrons, generated by the absorption of photons in Ge, move easily to n-Si and so a higher photocurrent can be detected (Figure 2.4). The final device is characterized by different patterns in which different parameters are changed such as: the distance between the microcrystals at the beginning of growth (G), the width of the gap between the patterned and the non-patterned region (D) and the width of the pillar itself (W) (Table 2.1, Figure 2.5).

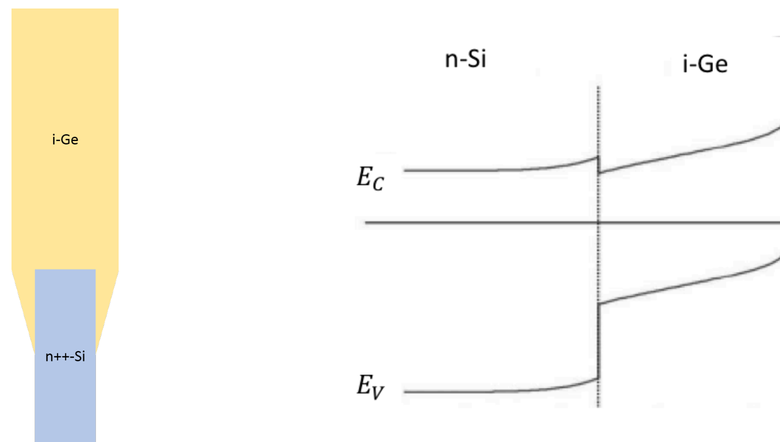

Figure 2.4: On the left the structure of i-Ge micro-crystals. On the right a representation of the band diagram at the interface between n-Si and i-Ge.

Pattern	W (µm)	G (µm)	D (µm)
A	2	2	2
B	2	3	3
C	2	4	4
D	3	3	3
E	4	3	3
F	2	2	4
G	2	3	6
H	2	4	8

Pattern	W (µm)	G (µm)	D (µm)
I	3	3	6
J	4	3	6
K	2	2	8
L	2	3	9
M	2	4	16
N	3	3	9
O	4	3	9

Table 2.1: Patterns characteristic dimensions.

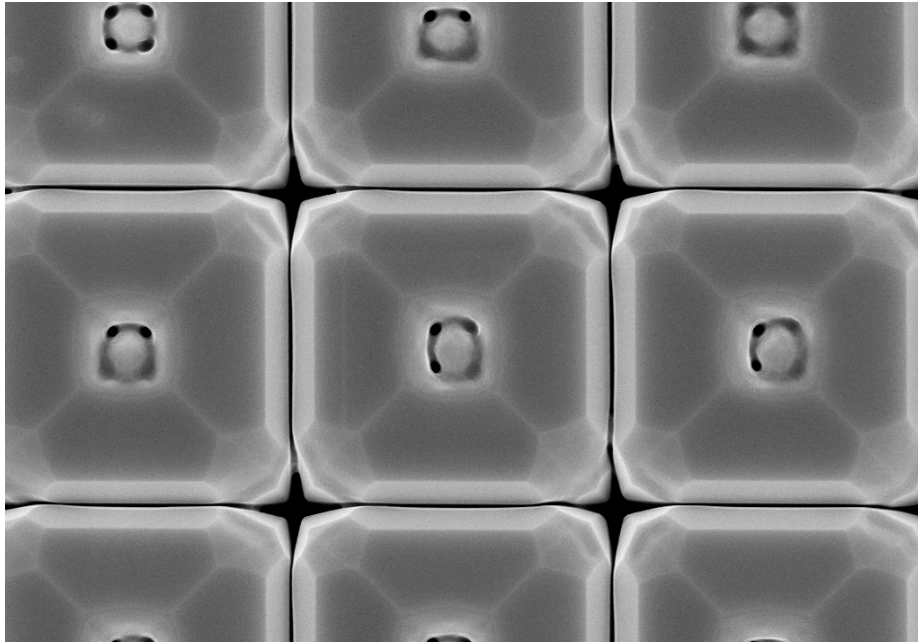

Figure 2.5: SEM images of the pattern A after growth.

2.4 Fabrication Process

As we have already mentioned the fabrication process is a critical aspect, in particular the realization of the contact of these Ge microcrystals which is needed to measure the photocurrent and to quantify device responsivity. The type of top contact implemented in this work is a transparent contact at the top of the pillars, such that a front illumination is possible. To deposit the ohmic back contact, the sample was placed on a copper plate. The main problem of this contact implementation is how to achieve a top contact that manages to be compliant with the three-dimensional shape of the pillars, their facets and the gap that is between them ranging from 50 nm to 1 micrometer depending on the pattern geometry. For these reasons

graphene was chosen as top contact. Graphene is able to adapt to the shape of the micro-crystals and to work as a transparent contact given its absorption of 2.4%.

Before carrying out the transfer of graphene the substrate must be prepared. In particular first of all the device, made by a patterned region of microcrystals i-Ge /n-Si and a non-patterned region of Ge/Si (Figure 2.6 (a)), was coated with an oxide layer of SiO_2. This was deposited, partially, by plasma enhanced chemical vapor deposition (PECVD) and partially by e-beam evaporation (see Appendix B.2), for a total of a thickness of 300 nm (Figure 2.6 (b)).

After that, a first step of optical lithography was done. The sample has been spin coated with negative photoresist AZ Nlof 2035 for a time of 60 seconds at a speed of 2500 rpm, reached with an acceleration of 500 rpm/s. It was baked on a hot plate at 110°C for 60 seconds to remove the solvent in excess and then a proper mask (Figure 2.7) have been used in order to transfer the pattern on the chip, exposing the photoresist with the UV emission from the Hg arc lamp of a Karl Suss MA56 mask aligner. After exposure, a baking at 110°C for 60 seconds on a hot plate was performed, and then the sample was placed in AZ 726 developer for one minute and fifteen seconds. This fabrication allows to have a window in the photoresist in the region where the micro-crystals are, while protecting the non-patterned area. In this way the photoresist protects the insulator in the unpatterned aerea. The SiO_2 layer, covering the pillars, has been removed by means of HF:H_2O 1: 5 solution, in which the sample was placed for 2 minutes (Figure 2.6 (c)).

Another lithographic step is necessary in order to define the top contact metallic pads, used to contact graphene with the external circuit by means of a micro-probe.

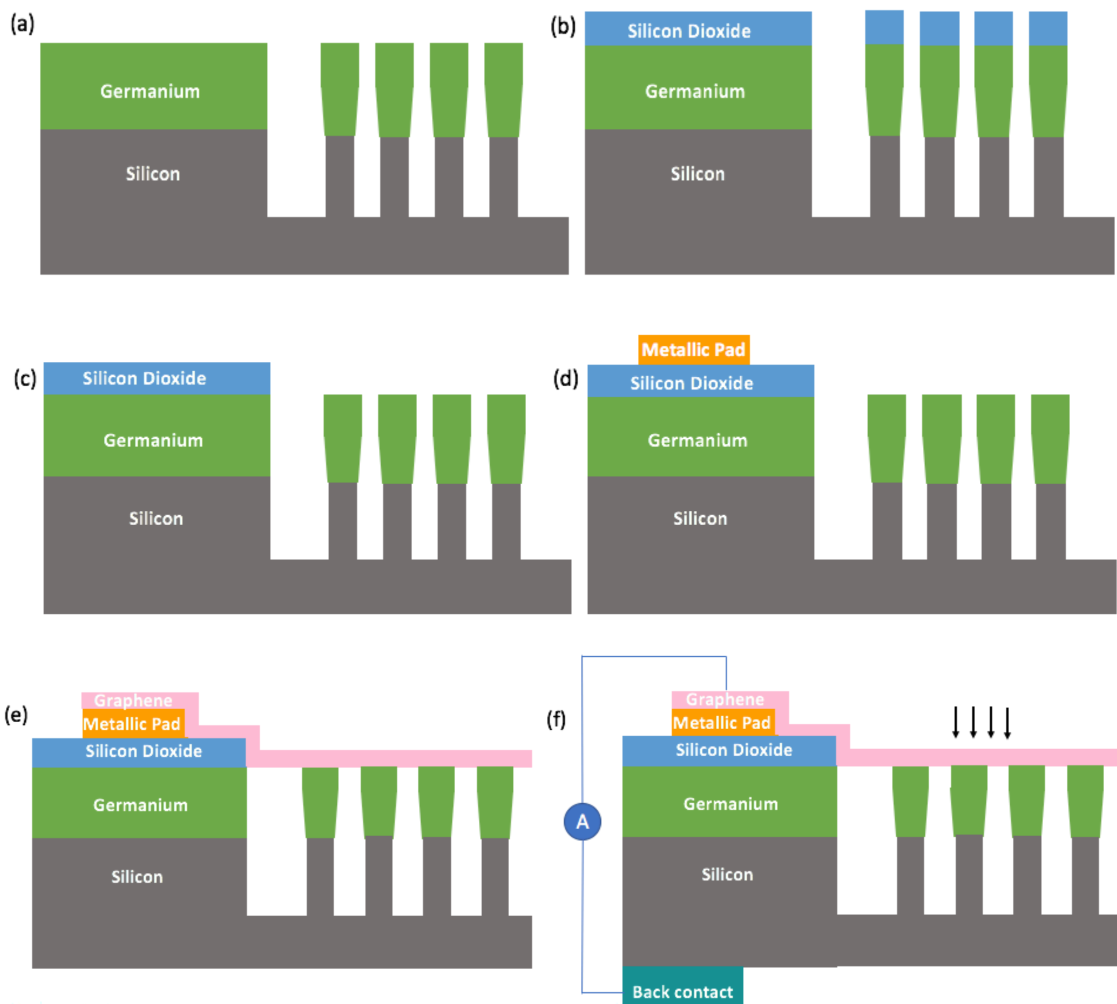

Figure 2.6: (a) Growth sample; (b) deposition of SiO_2; (c) removal of the silicon dioxide in the patterned region; (d) generation of the metallic pad; (e) graphene transfer; (f) final device structure;

A positive photoresist was used for contact deposition, requiring a different spin coating process which is of the duration of 60 seconds at a speed of 3800 rpm, reached with an acceleration of 500 rpm/s. After 10 minutes of waiting time, required for rehydration, the sample is baked on a hot plate at 110°C for 2 minutes. Before exposure a resting time of 10 minutes is required for thermal strain relaxation.

The next step consists in the exposure with the appropriate mask and with the development by placing the sample in AZ 726 developer for 3 minutes and 30 seconds. After development, a 200 nm metal layer made of Au/Al/Ti has been evaporated and then the so called lift-off process is performed. In this process the sample is placed in acetone for 4 hours, in such a way that the evaporated metal was lift off by the removal of the photoresist polymer which is below it, while in the regions where the photoresist is absent the desired metallic contact remains (Figure 2.6 (d), Figure 2.8 and Figure 2.9).
After these fabrication steps is possible to proceed with the graphene transfer, that will be analyzed in detail in the next section, and so the realization of the final device structure for the subsequent characterization (Figure 2.6 (e)/(f)).

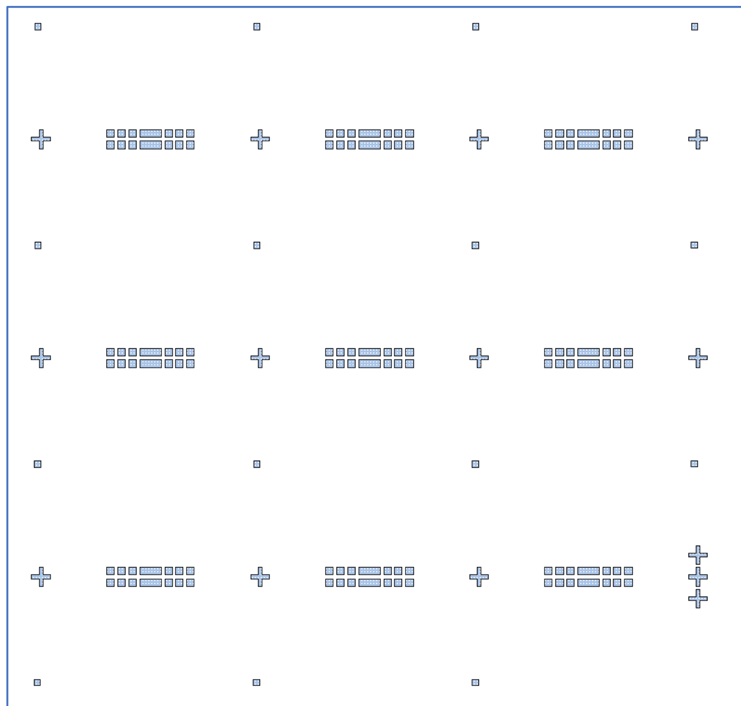

Figure 2.7: Mask used for the first optical lithography step.

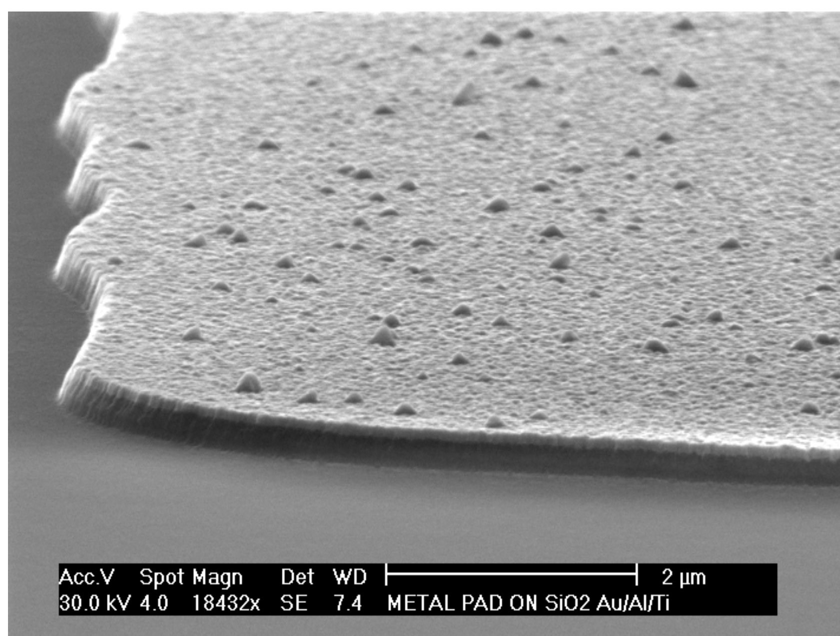

Figure 2.8: SEM image of the metallic pad of Au/Al/Ti on SiO_2.

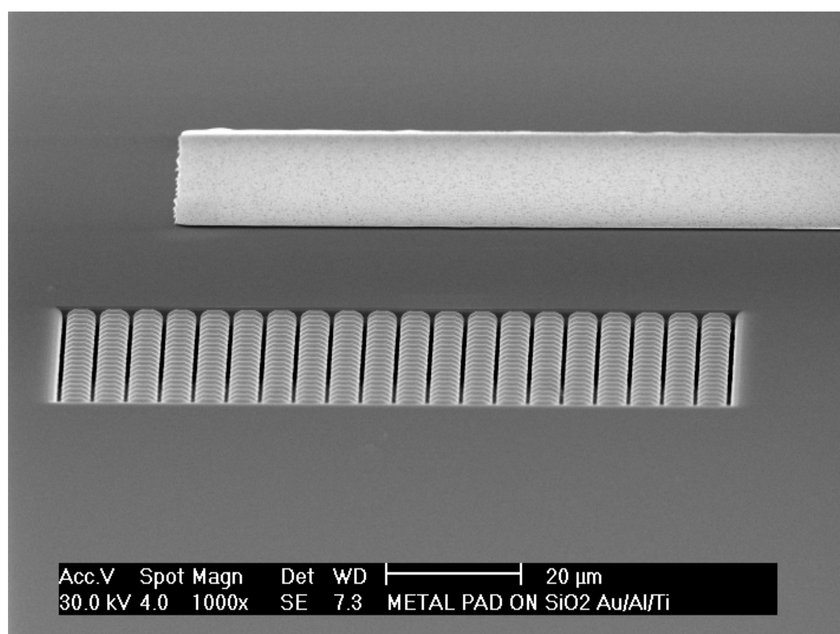

Figure 2.9: SEM image represented the metallic pad and the micro-crystals pattern.

2.4.1 Graphene Transfer

On the fabricated chip, I performed the transfer of graphene, which is a commercial CVD graphene grew on both sides of a copper foil, so, to obtain a self standing graphene layer, copper must be removed. In general the graphene wet transfer procedure consists of several steps, in which the graphene layer is kept floating in the different solutions:

1. A PMMA layer is spin coated on the top graphene at a velocity of 1000 rpm, achieved with an acceleration of 200 rpm/s for 60 seconds, followed by 2 minutes at 160°C on a hot plate. This PMMA layer is required to provide a mechanical protection and support for the graphene layer in the next steps.
2. The graphene on the bottom surface of the copper foil is removed by plasma Asher (see Appendix B.3) with a power of 500 W and a O_2 flux of 250 ml/min for 1 minute.
3. The Cu is etched by means of two successive solutions:
   - $HCl: H_2O_2: H_2O$ in concentration 1:1:5 for 45 seconds;
   - $FeCl_3: H_2O$ in concentration 1:2 for 4 hours;

   Graphene is “fished” from both solutions by means of a glass slide and rinsed by placing it in a beaker of deionized water. The rinsing procedure is repeated for at least 5 times in order to remove contaminating particles. Eventually, the micro-crystal sample is used to fish the flake out of the water. After 10 hours the water evaporates naturally and the graphene adheres to the substrate. To ensure a better adhesion, the sample is placed on a hot plate at 160°C for 5 minutes.
4. The PMMA layer is removed. This is typically performed by dipping the sample in acetone.

A sketch of the wet transfer process is represented in the Figure 2.10.

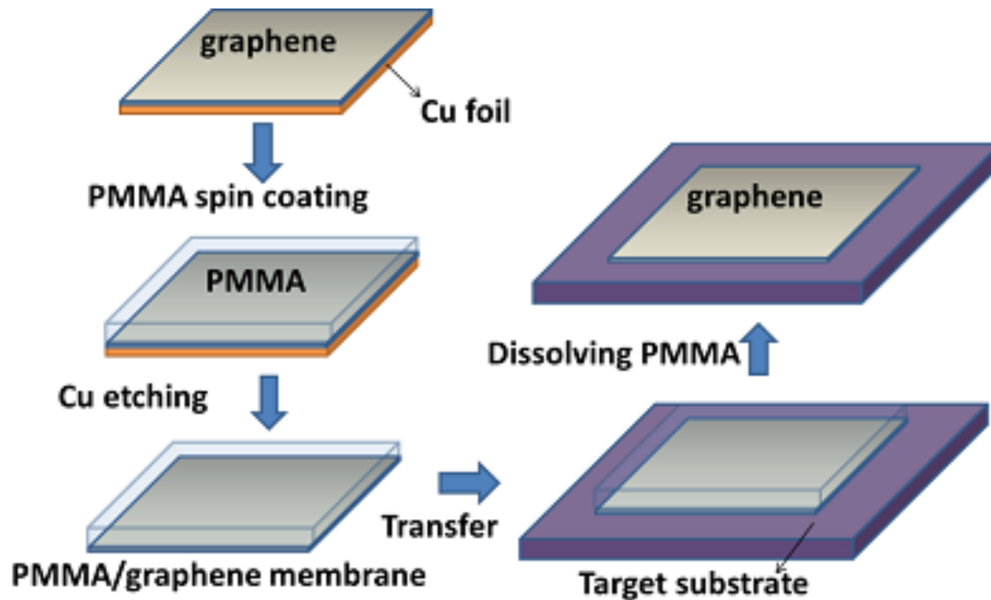

Figure 2.10: Representation of the different steps of the graphene transfer.

The obtained sample was then observed by SEM, to check the quality of the transfer. Unfortunately, the graphene layer obtained following this procedure was cracked and not continuum over the micro-crystals. Thus, a good transparent contact was not achieved by following the standard wet transfer procedures.

The reason behind such a bad outcome could be the effect of the capillary forces that play an important role for this type of patterned substrate in which the distance between the pillars is the order of μm. It has been observed that up to the third step of the process the graphene layer remains continuous, but then after the removal of the PMMA by acetone graphene breaks at the boundary between the patterned and the non-patterned region and inside the pattern itself generating a “spider web” effect (see Figure 2.11).

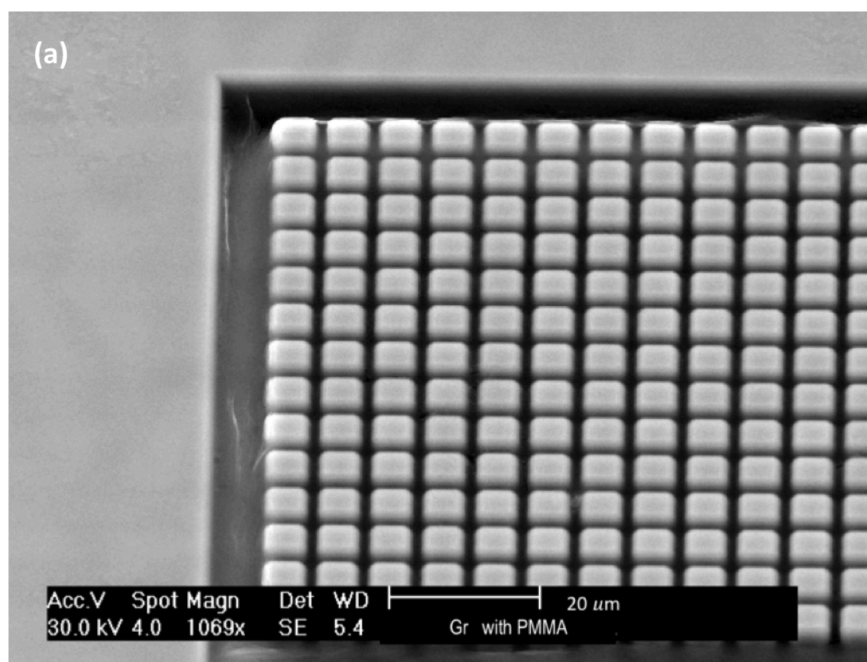

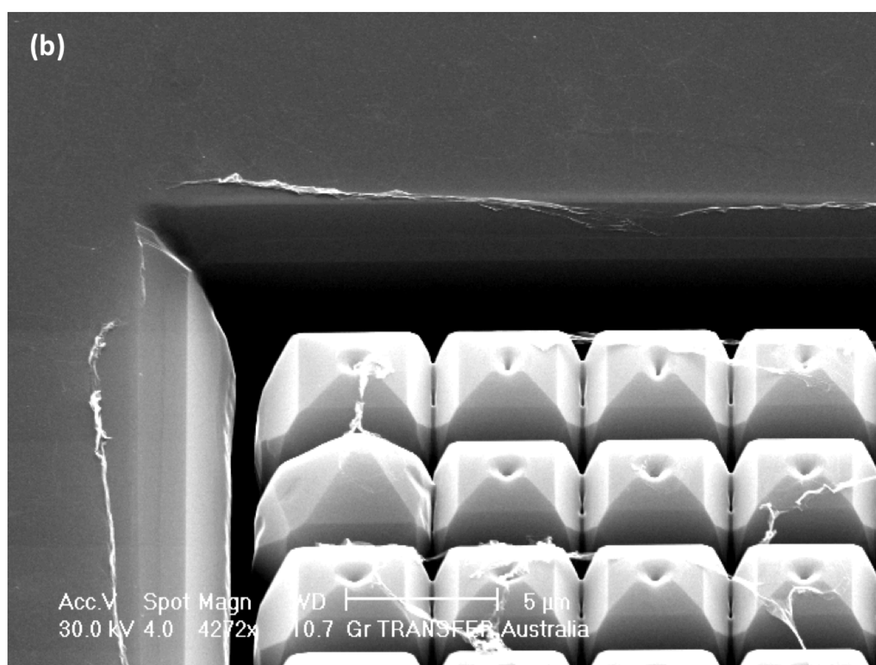

Figure 2.11: (a) Graphene with PMMA on the patterned region;
(b) Graphene after the removal of the PMMA.

2.4.2 Optimization of the Graphene contact

Due to the unsatisfactory results obtained by transferring a graphene monolayer, different strategies have been tried to optimize the process. Starting from the observation of the different steps of the transfer it seemed that the critical step was the PMMA removal, so I focused the attention on this step, trying to find a proper solution to keep the graphene layer intact.

2.4.2.1 SOG (spin-on-glass) oxide

An attempt was made to increase the mechanical support of graphene by trying to fill the gap between the micro-crystals.
For this purpose it is possible to use a spin-on glass (SOG). The spin-on glass used was diluted in isopropyl alcohol (IPA) with a 2:1 concentration and was spin coated at a speed of 1500 rpm. After deposition, it must then be removed from the top of the micro-crystal to allow contact with graphene. This can be achieved either by a dry type etching technique, such as RIE, or a wet technique with the use of a HF solution. Experimentally, however, we observed an insufficient filling of the gap between the different pillars, which makes this technique inefficient to support the graphene layer (Figure 2.12).

2.4.2.2 Optimization of the PMMA removal

Subsequently we tried to modify the technique used for PMMA removal, being a critical aspect of the process. Three different alternative approaches have been tried:

1. Thermal decomposition of PMMA layer by heating the sample in the RTA (Appendix B.3) with a flux of N_2 for 10 minutes at a temperature of 450 ° C.
2. Sample always in RTA but now with a reducing atmosphere of H_2 diluted in Ar for 30 minutes at 400°C.
3. Sample annealed in a vacuum oven at a temperature of 450°C and at a pressure of 10^{-7} mbar for 5 hours.

The sample was then observed by SEM for each of the three cases (Figure 2.13 and 2.14). Despite a slight greater extension of the suspended graphene by means of method 1, it was not possible to obtain a continuous suspended graphene layer that would allow contacting a significant number of pillars, necessary for the subsequent electro-optical characterizations.

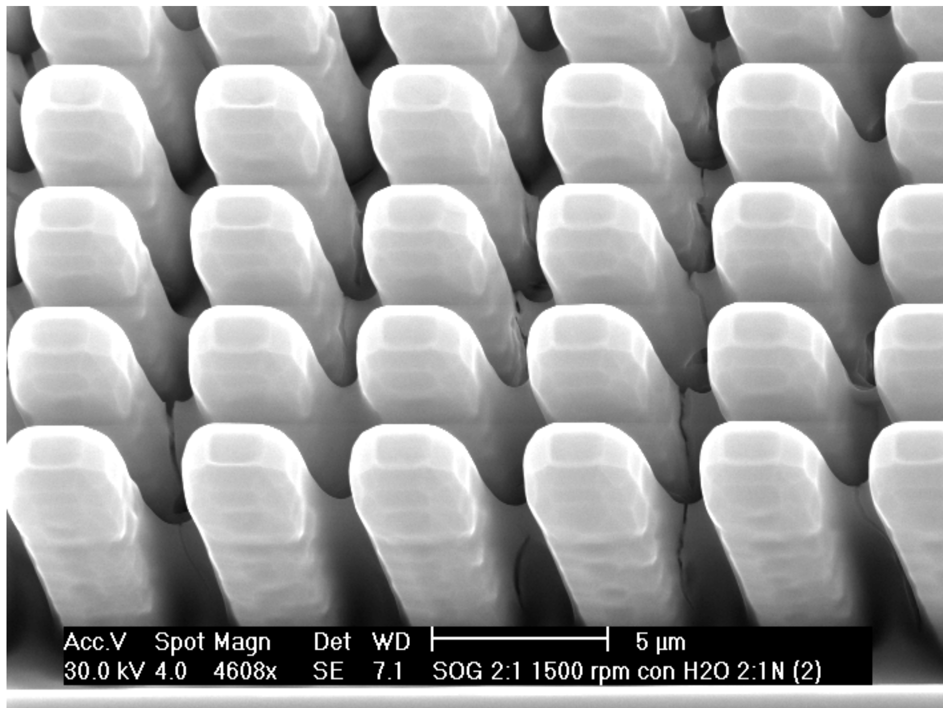

Figure 2.12: SEM image of the pattern post filling with SOG.

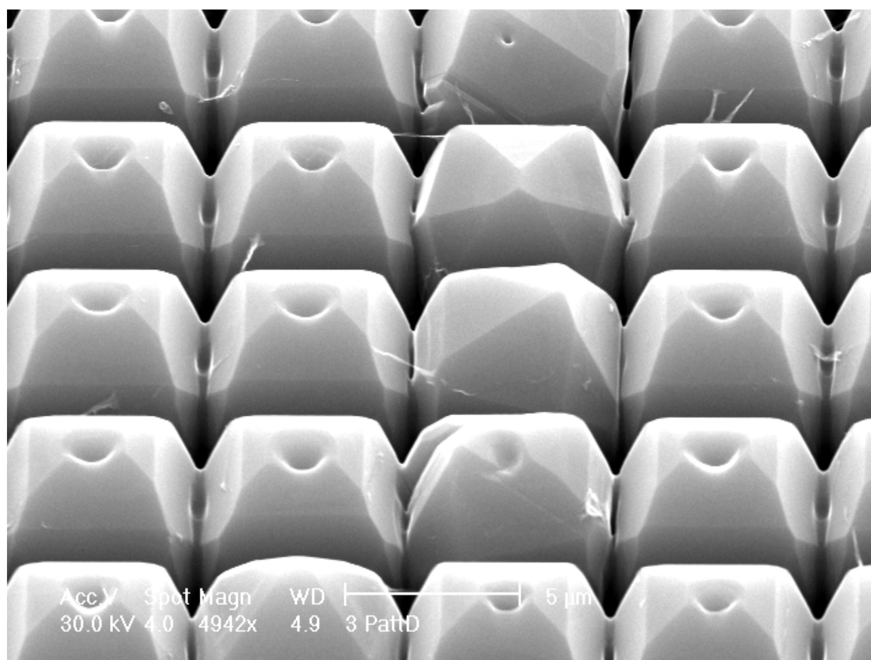

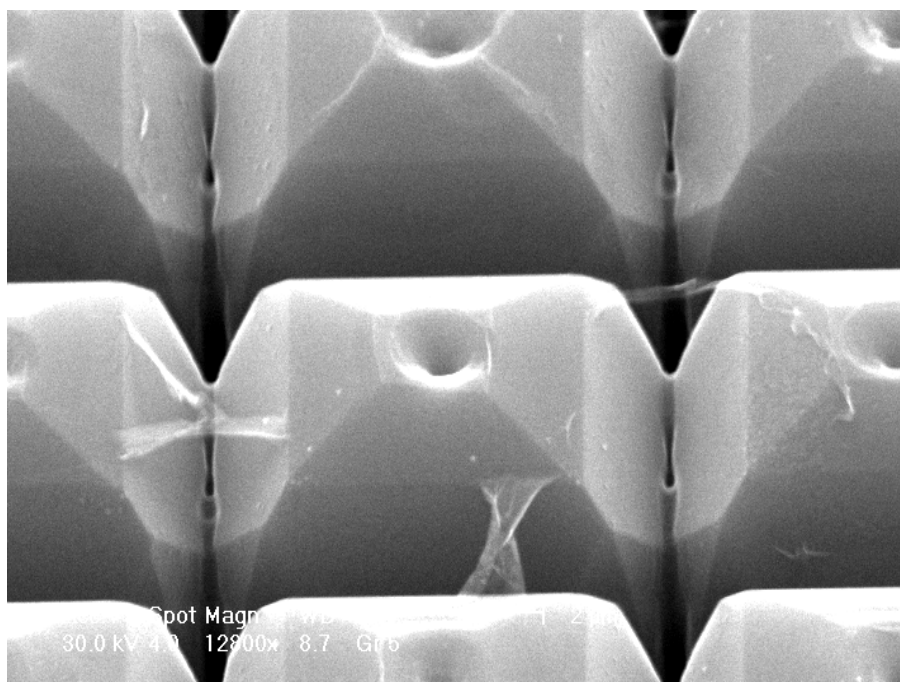

Figure 2.13: (a) Graphene on Ge micro-crystals after the PMMA removal with the vacuum oven; (b) Graphene on Ge micro-crystals after the PMMA removal in the RTA with the Ar and H_2 flux.

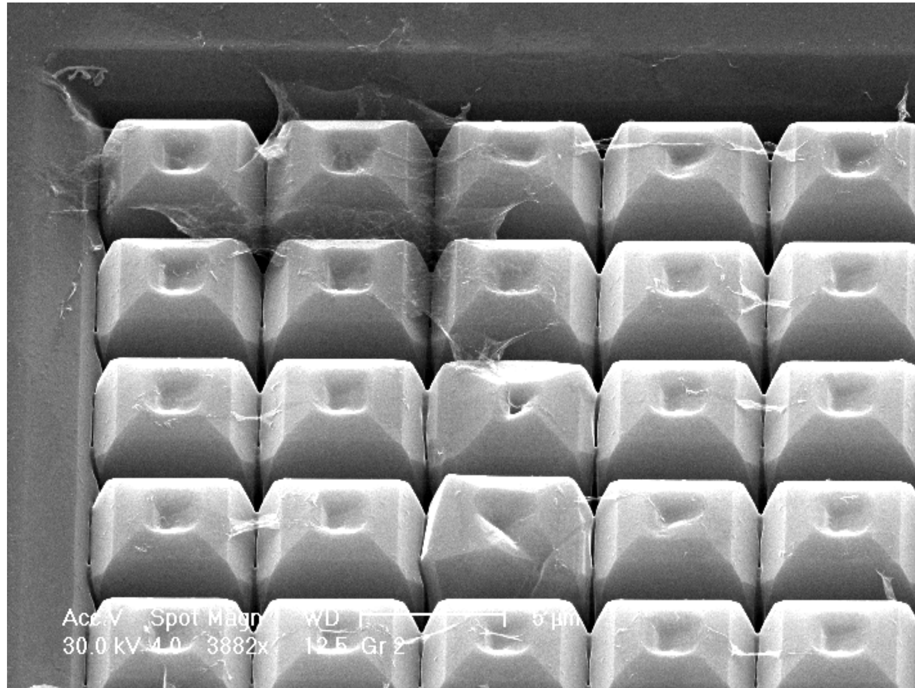

Figure 2.14: Graphene on Ge micro-crystals after the PMMA removal in the RTA with the N_2 flux.

2.4.2.3 Increasing graphene resistance

The modification of the final step of the transfer did not produce any improvements in the graphene quality, so I focused the attention on the increase of the graphene mechanical resistance. To do this I tried to make a contact not only with graphene but also through Au. In detail on a Gr/Cu chip it was carried out the evaporation of Au with a thickness of 7 nm and after all the process of Cu removal have been carried out, the graphene with Au was transferred on the sample. The thickness of the metal layer was chosen not to reduce the transparency of the top transparent contact too much. However, a non-homogeneity of the metallic layer of this thickness was observed, which did not allow the generation of a uniform contact. In fact, after

PMMA removal, the Au/Gr layer collapsed around each single pillar (Figure 2.15).

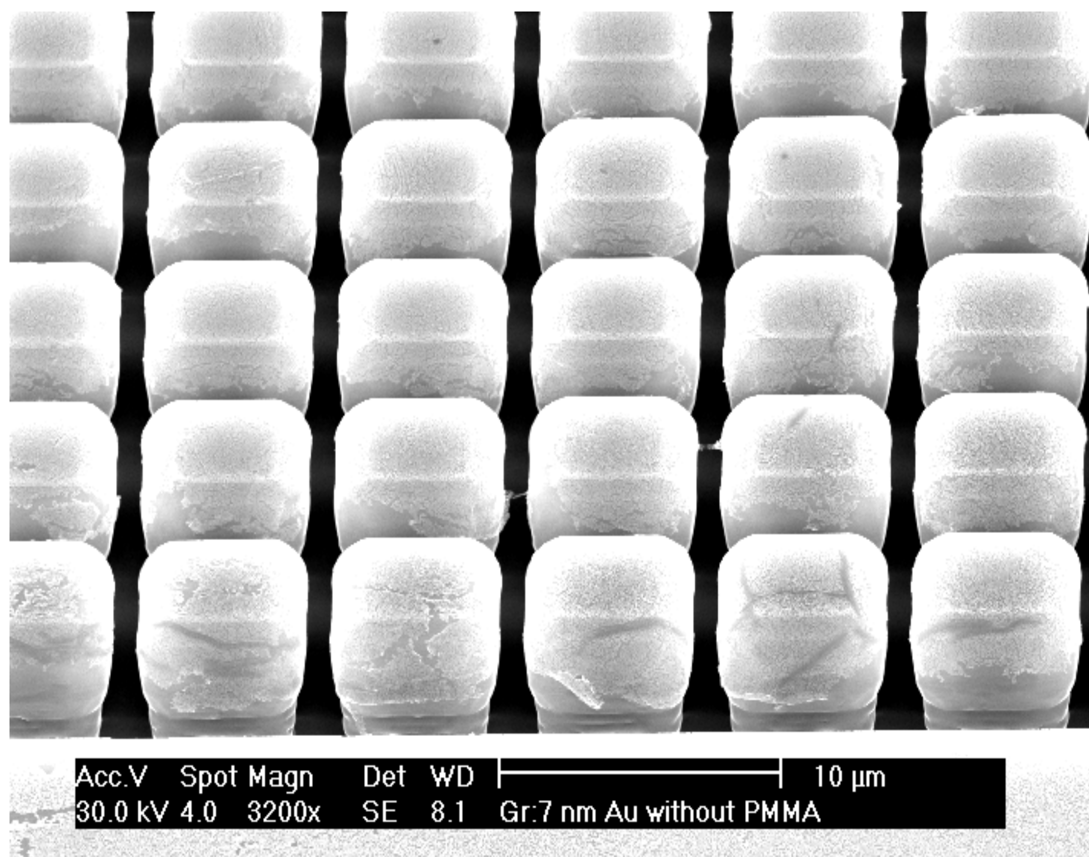

Figure 2.15: Graphene with 7 nm of Au after the removal of PMMA.

Consequently, it was decided to increase the resistance of the suspended graphene not by means of another material but rather by increasing the number of graphene layers used as a contact.
Specifically, a graphene bilayer was obtained by modifying the transfer process. In fact, once Cu was removed with the standard process, the single graphene layer was fished with another Gr/Cu chip. The Graphene bilayer then undergoes the standard wet transfer steps and finally this graphene bilayer flake was fished with the sample. After the drying process, PMMA was removed by means of

acetone, keeping the sample in vertical position. This process leads to the generation of a suspended bilayer contacting the top of the micro-crystals, regardless of the characteristic dimensions of the pattern (see Figure 2.16 and 2.17). In this case the absorption due to graphene doubles, but in any case it is estimated to be around 5% and therefore will not significantly affect the efficiency of the optoelectronic device.

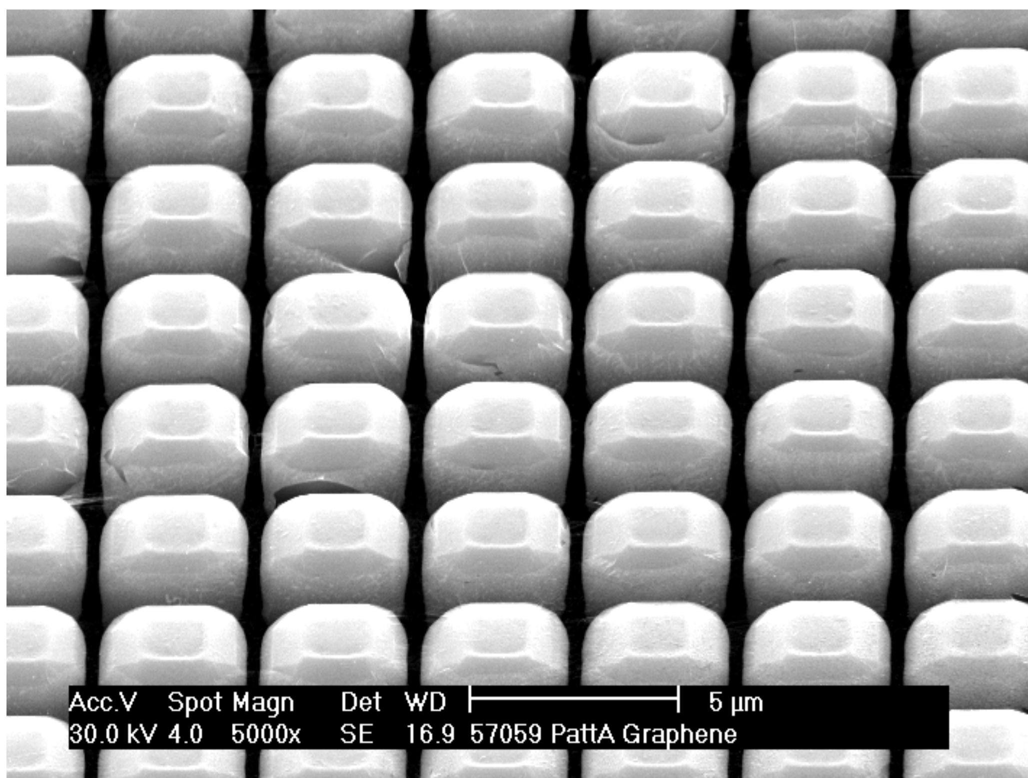

Figure 2.16: Bilayer of graphene on Pattern A with magnification 5000x.

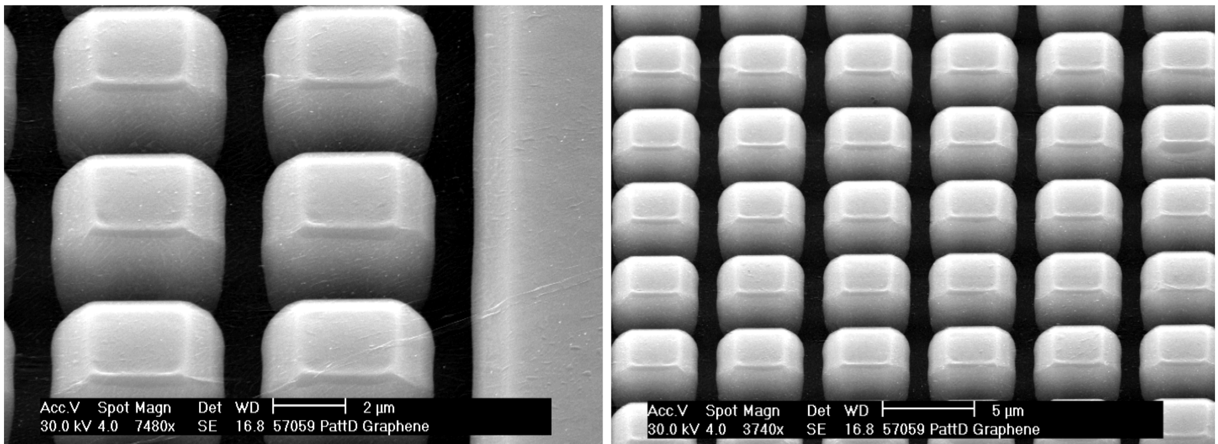

Figure 2.17: Bilayer of graphene on the pattern D, on the right SEM image with a magnification of 3740x while on the left image with a magnification of 748x.

Chapter 3

Electro-optical characterization

3.1 Experimental setup

The optical setup implemented to measure the photocurrent of the samples consist of a 100 W quartz-tungsten halogen lamp that is the broadband light source. A mechanical chopper, set at 391 Hz, is then used to modulate the light. A Oriel Cornerstone 260 monochromator, controlled by a Labview software, is used to select a single wavelenght of the spectrum, in order to be able to test the spectral response of the devices. The photocurrent generated by the samples is then collected and amplified by a transimpedence amplifier (TIA) and demodulated by a lock-in amplifier. The signal is then sent to a PC, which correlates it with the information about the incoming wavelength in order to obtain a spectrum. A scheme of the optical setup is shown in figure 3.1 The light beam is focused on the pattern of the device that we want to analyze.

An electrical probe, represented in Figure 3.2 (b), is used to land on the fabricated metallic pad for the top contact, while the sample is placed on a plate of Cu for the back contact connection. The terminals of the photodiode are connected to an external transimpedence amplifier (TIA), which amplifies and converts the photocurrent to a voltage signal and supplies the bias voltage. The input of the lock-in is AC coupled, to remove the DC component (i.e. the dark current), and is then demodulated using the reference signal supplied by the chopper. The signal is finally converted by an ADC and read by the LabView program running on the PC.

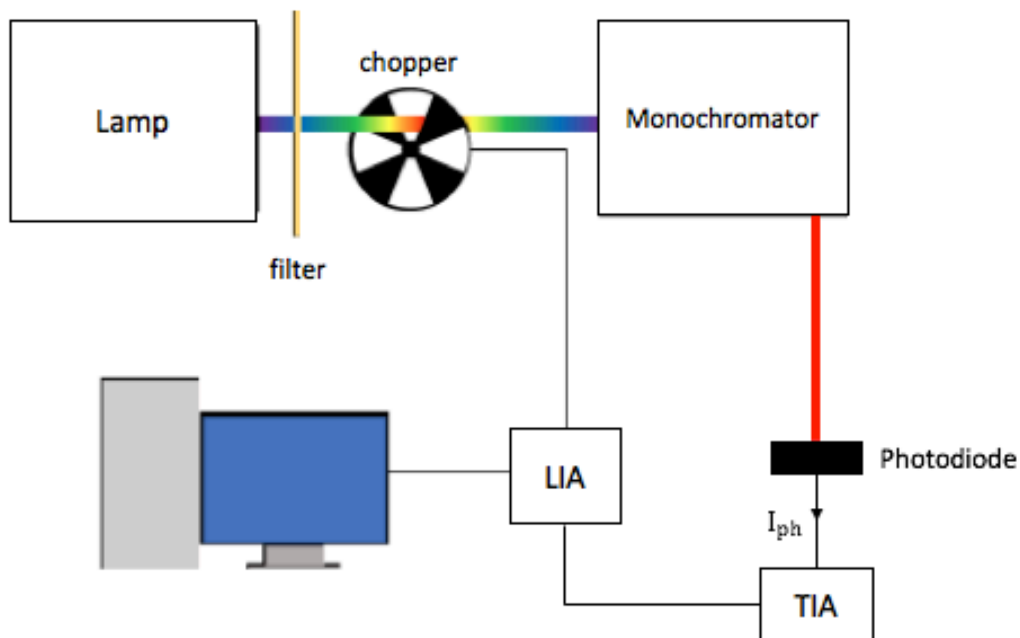

Figure 3.1: Representation of the experimental setup used for the electro-optical measurements.

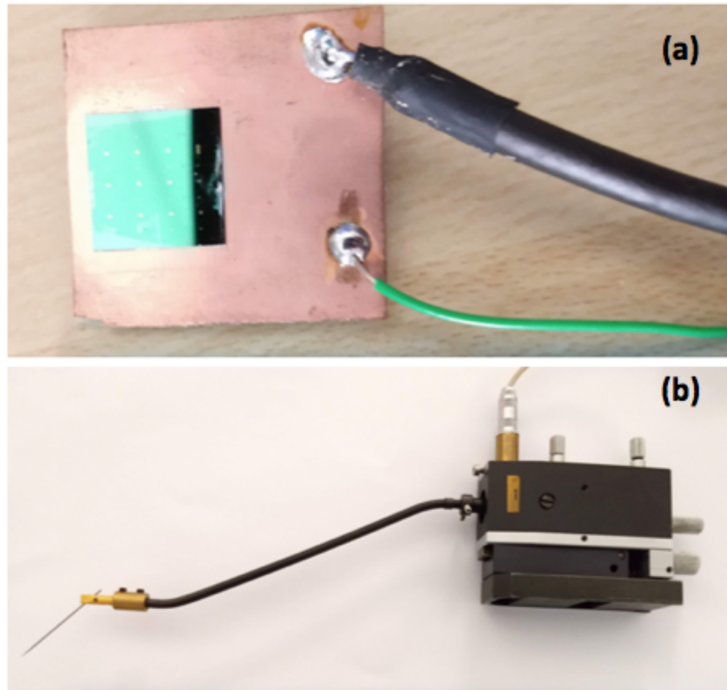

Figure 3.2: (a) Image of the sample on a Copper plate used for the back contact connection; (b) Probe used to land on the metallic pad for the electrical measurements.

Five different patterns have been investigated, namely: A, B, C, D and F and their morphology is shown in Figure 3.3. Before carrying out the various electrical measurements of interest, we wanted to verify the presence of a Schottky junction by means of I-V characteristics of the device measured with a source-meter unit. The results of this measurements are shown in Figure 3.4. The I-V characteristics for pattern A, D, J and F do not seem to follow the expected trend of a Schottky junction between the graphene and a semiconductor (see Figure 1.4). Probably this is due to the absence of any intentional doping of the Ge micro-crystals, which are non intentionally doped in this sample. It is also worth mentioning that in this set of samples the graphene layer covers the whole surface of the chip. This

multiplies the number of current paths, masking the electric behavior of the patterned region under investigation.

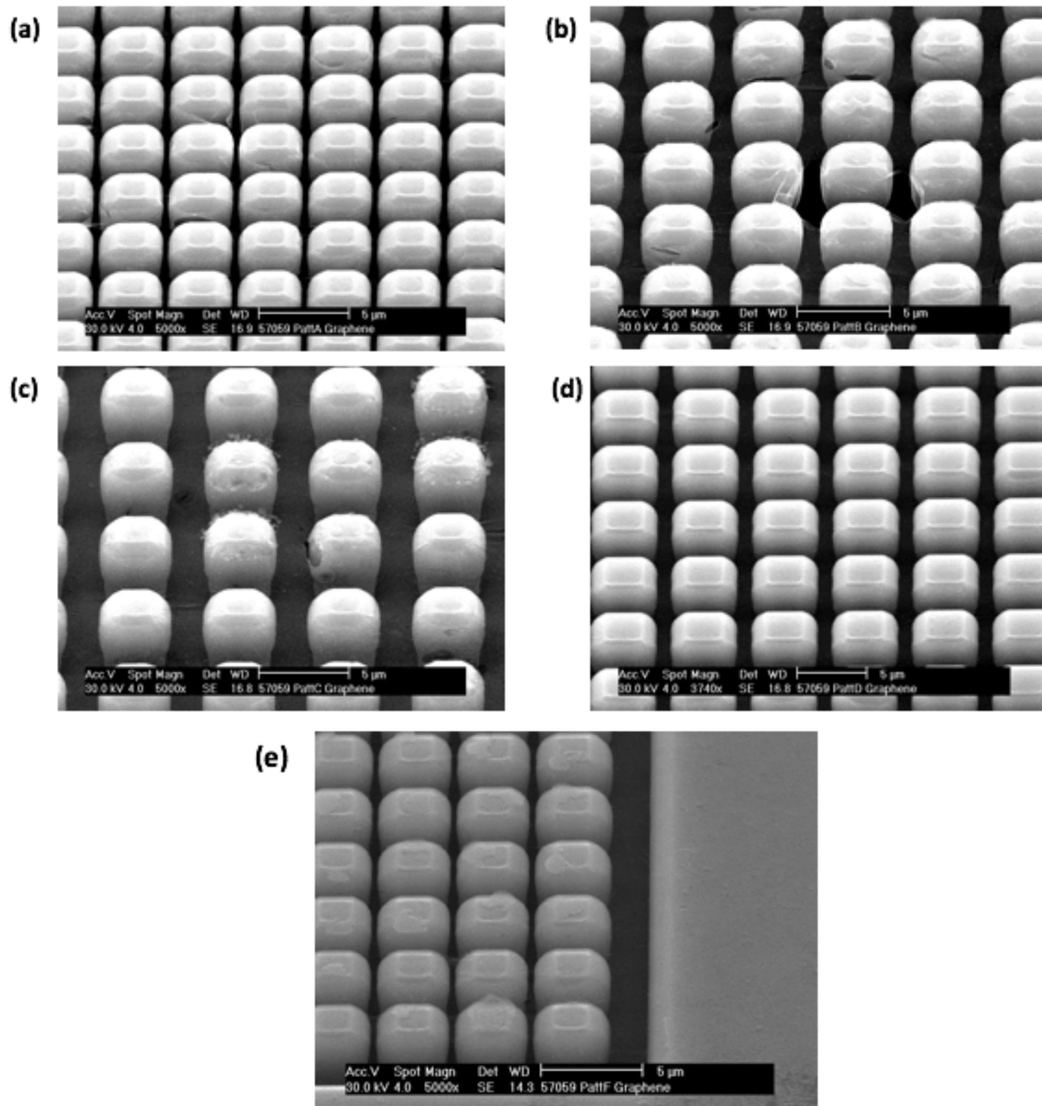

Figure 3.3: SEM images of the patterns used for the measurements: (a) pattern A; (b) pattern B; (c) pattern C; (d) pattern D; (e) pattern F.

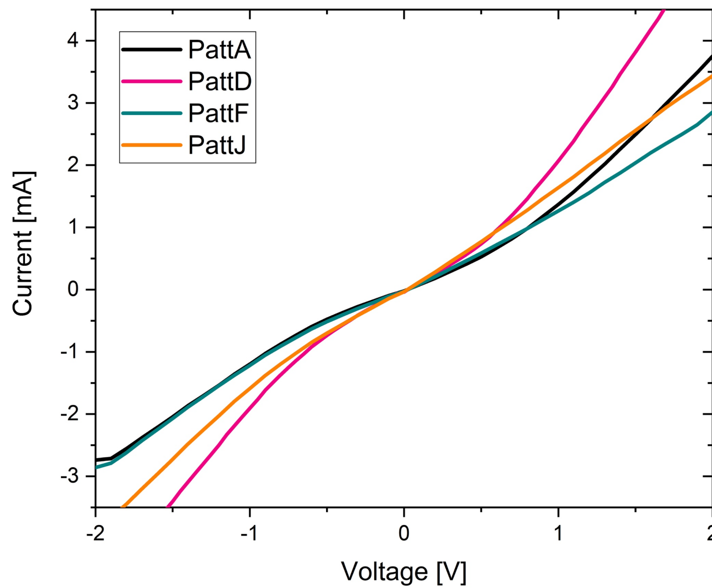

Figure 3.4: I-V characteristics for pattern A, J, D and F.

3.2 Photocurrent measurements

When the semiconductor is illuminated the absorption of photons leads to the generation of electron-hole pairs. The applied voltage on the detector, or the built in potential generated at the interface, is enough to separate the carriers, which travels to the respective contact. In this way a photogenerated current can be collected. It is also important to note that Ge micro-crystals can be made substantially thicker than a conventional epi-layer whose thickness is limited to approximately 4 µm due to the formation of thermal cracks. At the same time micro-crystal arrays feature a surface fill factor greater than 90%. This should lead to an efficient light absorption within the micro-crystals array.

The experimental photocurrent obtained for the pattern A, D and C are represented in Figure 3.5.

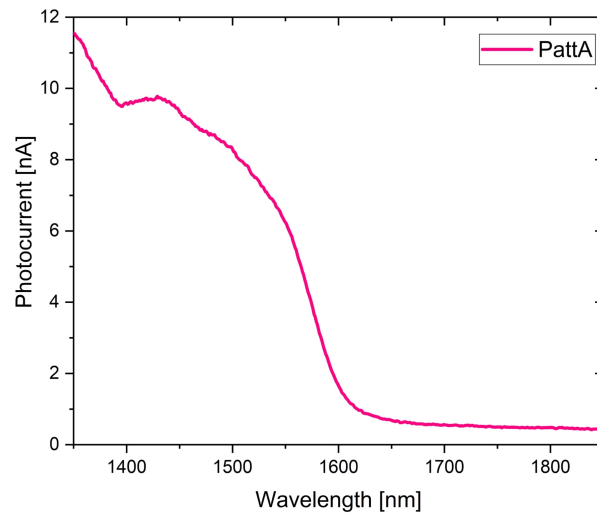

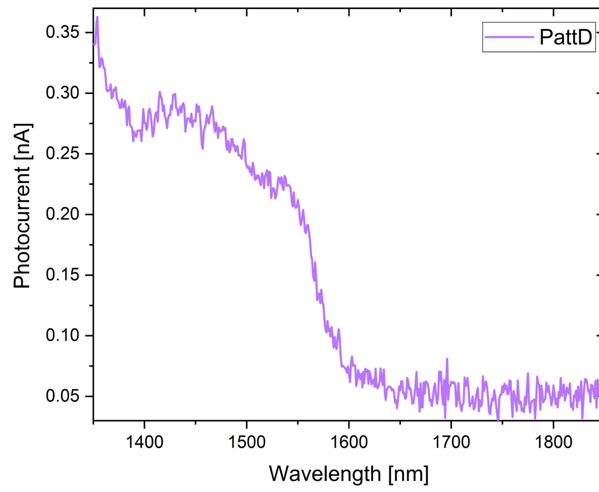

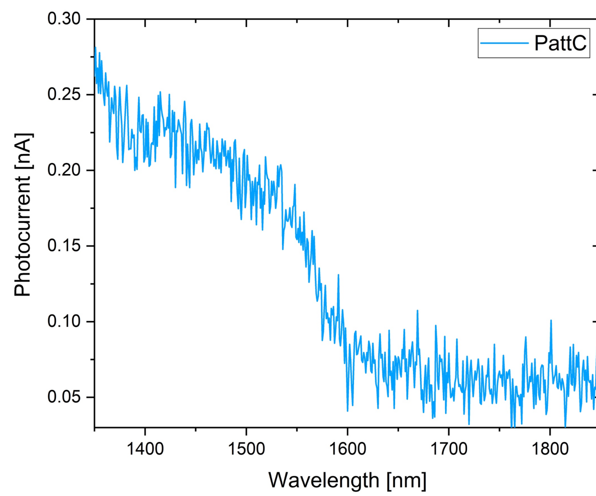

Figure 3.5: Photocurrent measurement of pattern A, D and C.

The use of a microprobe for the photocurrent measurements made the alignment between the light beam and the patterned region, which is only 100 µm wide, extremely challenging. For this reason the photocurrent intensity collected from different patterns varied by a few order of magnitudes as can be clearly seen in Figure 3.5, with clear consequences on the signal-to-noise ratio which is higher in sample with lower photocurrent. This could be due not only to the stability of the setup used but also to the possible lower quality of the graphene. This is for example the case of the pattern C where “stains” of PMMA are still present on the graphene that contacts the micro-crystals of Ge (Figure 3.6).

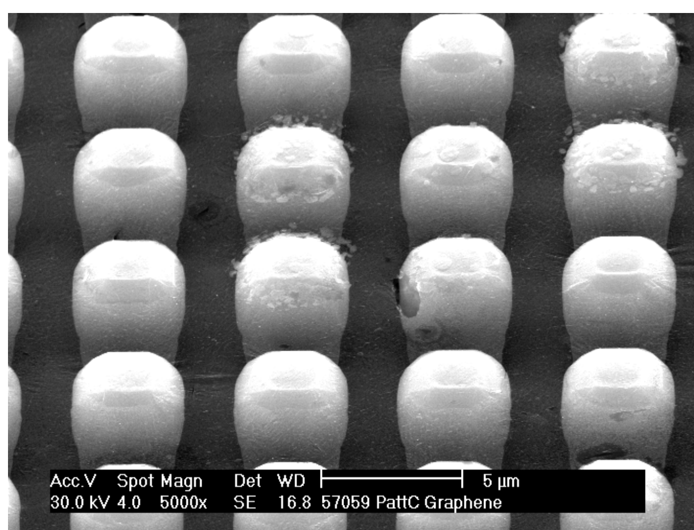

Figure 3.6: SEM image represented the PMMA impurity in the graphene layer of the pattern C.

Furthermore, to confirm that only the photocurrent generated in the patterned area is collected, a measurements of the non-patterned area, done by focusing the light out of the pattern, have been performed. The result is represented in Figure 3.7. It is possible to notice how in the non-patterned area what is measured is basically

just noise, while the only actual photocurrent signal is coming from the patterned area.

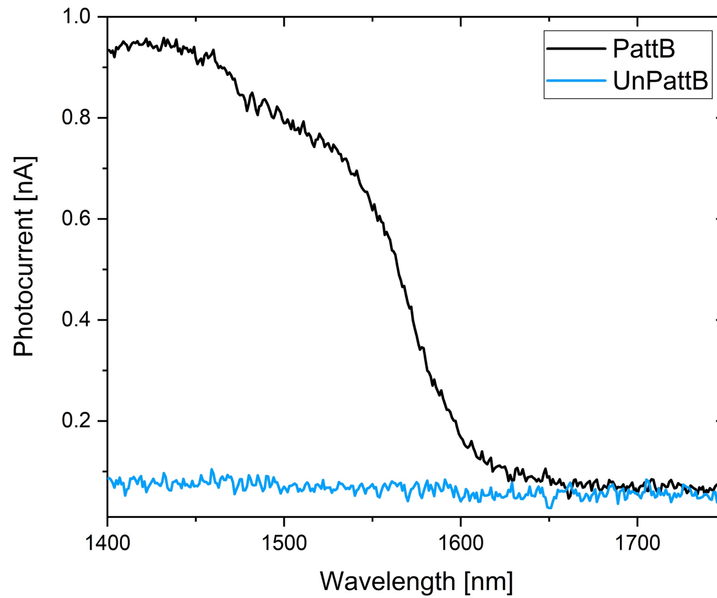

Figure 3.7: Measure of photocurrent of the pattern B and of the unpatterned area close to the pattern B.

The beam size obtained with the optical setup used for these measurements is substantially larger (approx. 1 mm diameter) than the patterned region, which makes a quantitative estimation of the responsivity essentially impossible. For this reason an evaluation of the responsivity has been performed using a confocal microscope set-up.

The use of a confocal microscope allowed to illuminate a limited region of pillars within the pattern and therefore to quantify the incident effective power, and consequently the responsivity (Figure 3.8). The responsivity obtained is approximately 20 times lower than what is typically obtained in Ge-on-Si photodetectors. In the next fabrication run we are planning to optimize the doping profile within the Ge micro-crystals to improve the responsivity, as will be better discussed in the "Conclusion and future works" section.

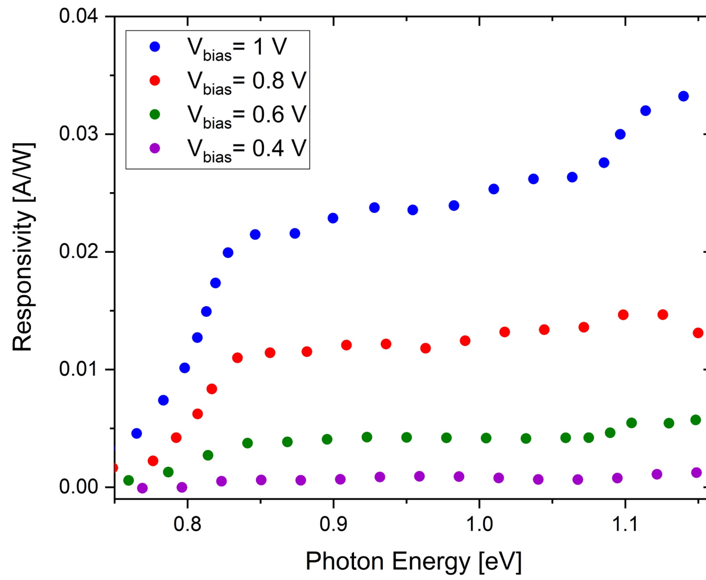

Figure 3.8: Responsivity obtained with a confocal microscope.

Moreover for all the different patterns, it is possible to notice the characteristic trend of the photocurrent given by the Ge direct absorption. In fact, approaching 1550 nm, the cutoff can be observed and the photocurrent collapses to almost zero (Figure 3.9). This trend will be better analyzed in the next section.

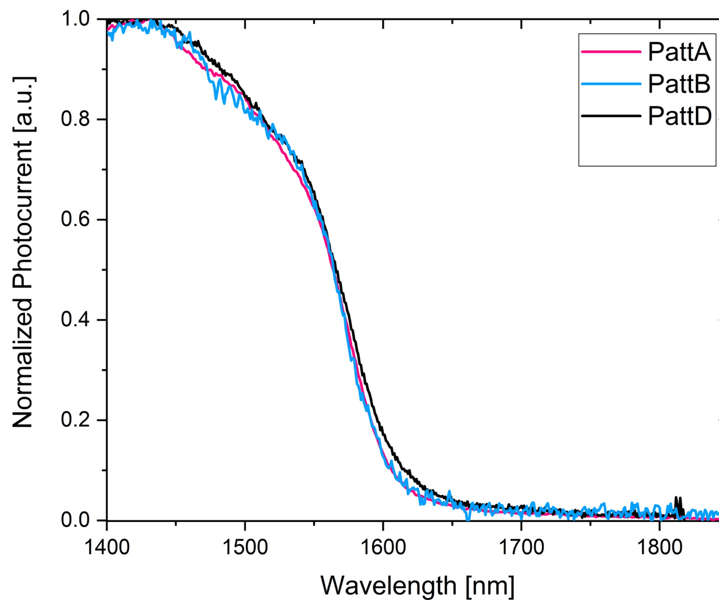

Figure 3.9: Normalized Photocurrent of patterns A, B and D.

3.3 Estimation of the energy gap

In the photocurrent measurements obtained for the different patterns is possible to note that the direct gap absorption of Ge dominates. This is due to the fact that the Ge micro-crystals thickness is not sufficient to give a sizable indirect absorption. For this reason it is possible to consider just the direct absorption, when analyzing the optical response of the devices.
The absorption coefficient for a specific photon energy is proportional to the probability of the photo-induced conduction band-valence band transition and to the density of states in the initial and final states. The transition must satisfy the energy and the total momentum conservation:

$$h\upsilon = E_f - E_i \quad (3.0)$$

$$k_f = k_i + k_{opt} \quad (3.1)$$

where $h\upsilon$ is the photon energy, E_i is the initial energy of the electron in the valence band and E_f is its final energy in the conduction band. While in the total momentum conservation k_{opt} is the field wavevector, k_i is the initial wavevector of the electron in the valence band and k_f is its final wavevector in the conduction band. Considering that $k_{opt} = h/\lambda$, where λ is the wavelength of the light, it is much smaller with respect to the electron momentum k_i and k_f, momentum conservation (Eq. 3.1) can be written as:

$$k_f = k_i \quad (3.2)$$

This equation tells that transitions between two electronic states must occur vertically in k-space as can be seen in Figure 3.10. By using the parabolic approximation for the dispersion curve is possible to write (ref [15]):

$$E_f - E_{gap} = \frac{\hbar^2 k^2}{2m_e^*} \tag{3.3}$$

Where m_e^* is the effective mass of the electron and E_{gap} is the energy gap of the semiconductor, while:

$$E_i = -\frac{\hbar^2 k^2}{2m_h^*} \tag{3.4}$$

is the energy of the initial state in the valence band.

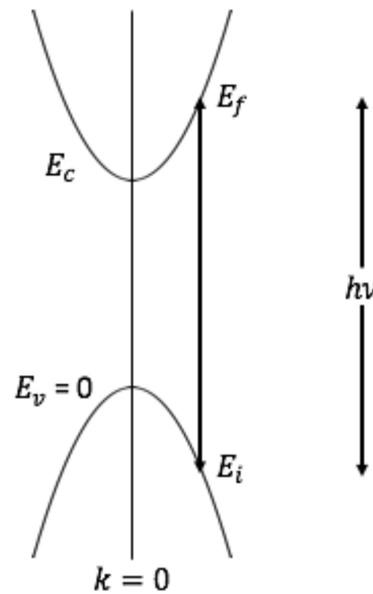

Figure 3.10: Vertical transition from the valence band to the conduction band.

In this way energy conservation (Eq. 3.0) can be rewritten as:

$$hv - E_{gap} = \frac{\hbar^2 k^2}{2}\left(\frac{1}{m_e^*} + \frac{1}{m_h^*}\right) \tag{3.5}$$

Considering this last equation and the dependence of the absorption coefficient on the density of states that for a direct transition can be represented by:

$$N(hv)\, d(hv) \propto (m_r)^{3/2}\left(hv - E_{gap}\right)^{1/2} d(hv) \tag{3.6}$$

The absorption coefficient can be written as:

$$\alpha(hv) \propto \left(hv - E_{gap}\right)^{1/2} \tag{3.7}$$

Using the previously described measurement setup we proceeded to estimate E_{gap} of the Ge micro-crystals by means of the measured external quantum efficiency (EQE), defined as:

$$EQE = \frac{I_{ph}}{e} \times \frac{\hbar\omega}{P} \tag{3.8}$$

It is possible, by knowing the incident power (P) of the beam on the pattern and considering the absorption of the photons in a thickness d with an absorption coefficient α, to calculate the number of electrons collected per unit of time (n_e) as in the Eq. 3.9:

$$n_e = \frac{I_{ph}}{e} \propto \frac{P}{\hbar\omega}\left(1 - e^{-\alpha d}\right) \tag{3.9}$$

Starting from Eq. 3.9, and considering Eq. 3.8, we can derive an inverse formula for the absorption coefficient:

$$\alpha \propto -ln\,(1 - EQE) \tag{3.10}$$

It is therefore possible to estimate the energy gap from the experimentally measured external quantum efficiency by combining Eq. 3.10 and 3.7. To do that we need to consider the region of the absorption curve close to the cutoff, and so the region in which the absorption coefficient is small. By doing this assumption it is possible to expand in series the exponential term of Eq. 3.9. As a consequence a direct proportionality between the absorption coefficient and the external quantum efficiency is obtained:

$$\alpha \propto EQE \tag{3.11}$$

It is therefore possible to rewrite Eq. 3.7 as:

$$(EQE)^2 (hv)^2 \propto hv - E_{gap} \tag{3.12}$$

To prove the validity of this approximation the two curves representing Eq. 3.10 and 3.11 for the pattern F were compared. The result is represented in Figure 3.11, in which a perfect overlap of the curves in the cutoff region occurs.

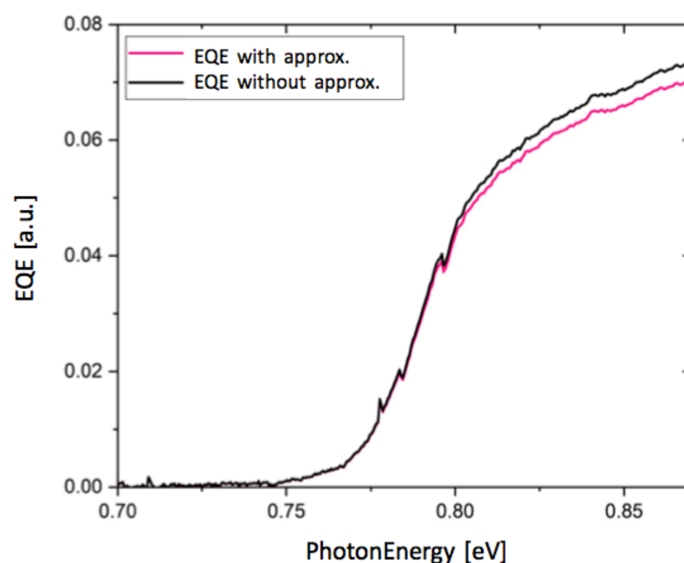

Figure 3.11: Proof of the validity of the approximation.

Representing graphically the experimental results of Eq. 3.12, it is possible to estimate the energy gap of Ge from the intersection between the straight extension of the curve and the abscissa.
This was done for patterns F and D (Figure 3.12 and Figure 3.13). For both patterns we estimated an E_{gap} of 0.78 eV.

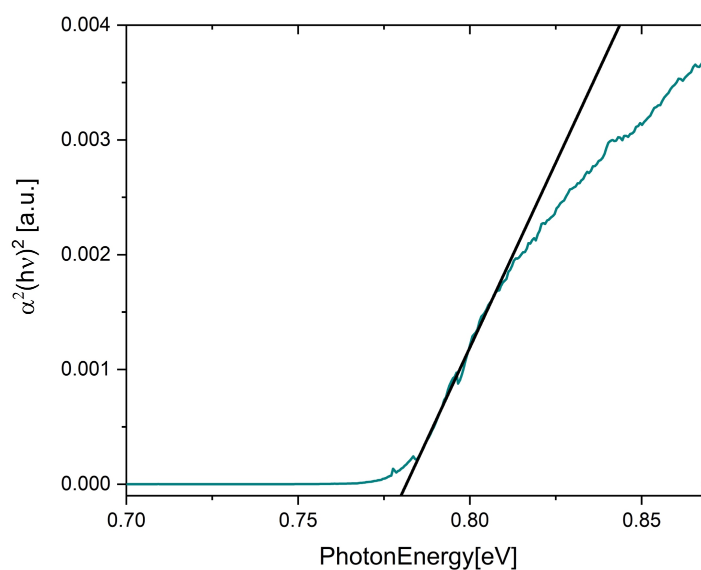

Figure 3.12: Estimate of the energy gap for the pattern F.

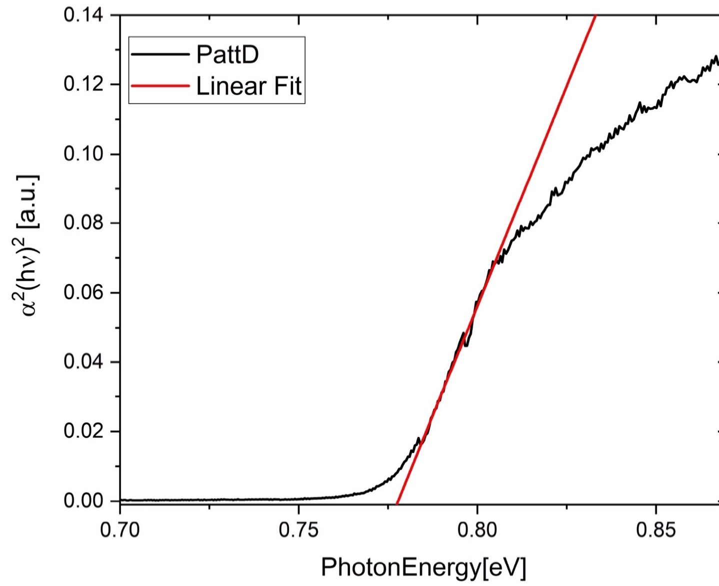

Figure 3.13: Estimate of the energy gap for the pattern D.

The energy gap of relaxed Ge is 0.803 eV so, despite these Ge micro-crystals of 8 µm height are expected to be completely relaxed, there is a shift of the E_{gap} to lower energies, an indication of residual tensile strain. By looking at Figure 3.3 we can notice that in this pattern the Ge microcrystals are well separated: this suggests that also the strained Ge deposited in the trenches between the Si pillars can contribute to the photocurrent, leading to a red shift of the energy gap.

3.4 Conclusion and future work

The fabrication of photodetectors based on Ge micro-crystals has been implemented with the use of graphene as a top transparent contact. By suspending a graphene bilayer it was possible to generate a continuous contact which adapts to the three-dimensionality of the

micro-crystals. The electro-optical characterization demonstrated the direct absorption of Ge and that the photocurrent signal comes clearly from the patterned area only. As a follow-up of this work we are considering an improved version of the photodetector with an optimized doping profile of the microcrystals.
By adding a p-type Ge contact on top of the structure, thus obtaining a p-i-n structure, it is possible to generate a depletion region that extends in all the intrinsic layer (Figure 3.14). This high extension of the space charge region increases the active area for the absorption of photons. This implies a consequent increase of the generation of electron-hole pairs, and so a higher photocurrent should be detected. Moreover the approach used to make the upper contact seen in this thesis could also be used for others materials such as Si and GaAs.

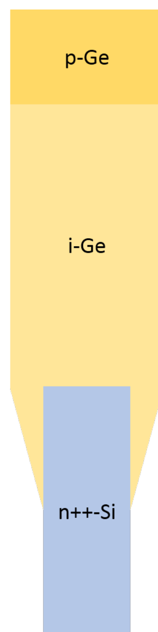

Figure 3.14: The structure of the optimal Ge micro-crystals made by top p-Ge/i-Ge/n++ Si.

Appendix A

1. Optical lithography

To perform the fabrication of the photodetector, lithography is required. In optical lithography a photo-sensitive polymer is used, called photoresist. The general steps of this procedure are represented in Figure A.1 and are carried out in this order:

1. Cleaning of the sample and dehydration bake to remove the water present on the substrate that can reduce the adhesion;
2. Spin coating on the substrate of a photoresist film of a specific thickness defined by the spinning time and speed;
3. Prebaking to dry the photoresist and remove the excess solvent;
4. Use of the mask aligner to align the photomask with the sample, and expose the sample to UV light;
5. Post-exposure baking promoting chemical reactions that remark the difference between the exposed and not exposed region;

6. Development of the photoresist by means of a chemical developer AZ 726MIF;

In particular, as represented in figure A.1, it is important to define the difference between two general types of photoresist that can be used: the negative and the positive one.

The difference between them is defined by how they are influenced by the incident light. In particular in the case of the positive photoresist the regions that are exposed to the UV light will change their chemical bonds, and the photoresist becomes more soluble during the development step.

Instead the negative photoresist works in the reciprocal way.

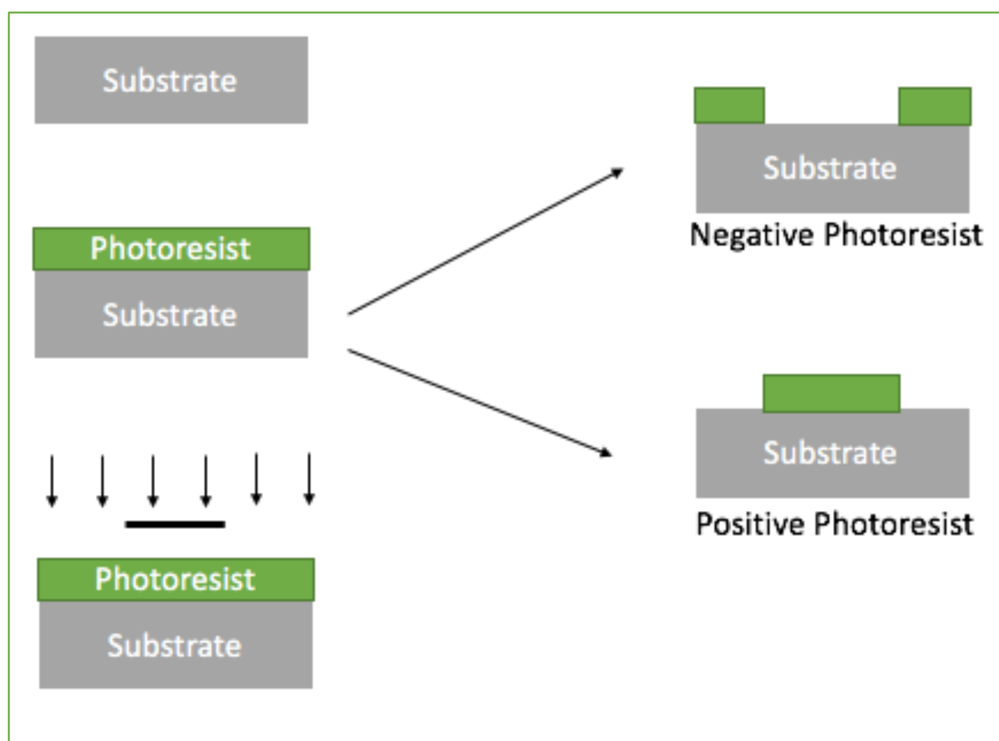

Figure A.1: Sketch of the optical lithography process.

Appendix B

1. Cryogenic deep RIE

The reactive ion etching (RIE) is a dry etching technique, based on the anisotropic etch of the sample. In the RIE machine (Figure A.2) the sample is placed at the bottom of a vacuum chamber, while a flux of gas enters from the top of the chamber itself and it is used to perform the etch process. The type of the gas used and its amount depends on the particular sample that needs to be etched. In particular in the case of a silicon substrate SF_6 is used. By the application of a RF voltage at the wafer plate a plasma is generated, and the electrons accelerated by the RF field reach the chamber walls and the wafer plate. In this way, negative charges accumulate on the plate, which attract the ions of the plasma. Some of these ions chemically react with the sample leading to an isotropic etch, while others sputter-off the substrate material in an anisotropic way. In particular in the case of a cryogenic deep RIE usually the wafer plate is maintained at a temperature of 163 K. This low temperature inhibits the chemical reactions, implying

just an ionic bombardment of the substrate that guarantees the generation of a vertical etch of the sidewalls.

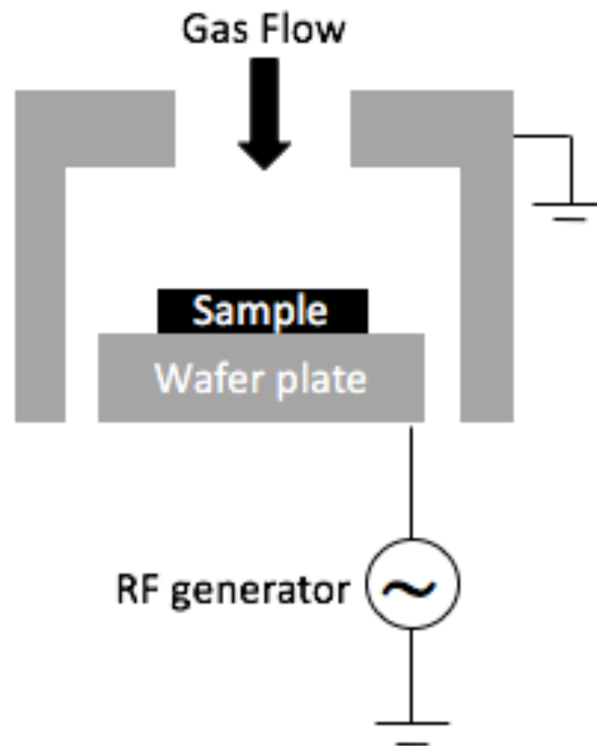

Figure B.1: RIE machine sketch.

2. Electron-beam evaporation

Electron beam evaporation is used to deposit different materials, such as oxide and metals. In the evaporator the sample is placed inside a vacuum chamber and the process of evaporation starts at a pressure of the order of 10^{-6} mbar. Inside the chamber the sample is mounted in the upper part with the top face facing down. At the bottom there is a tungsten crucible in which there is the material to be evaporated.

This last one is bombarded by electrons, that are generated by thermionic emission from a heated filament, and are accelerated and deviated from their source by a magnetic field.
By means of electronic bombardment a gas formed by the atoms of the target is made, that then will precipitate into the solid form on the sample. In particular the evaporator used for the sample of this thesis is a a Leybold Heraeus L 56 of the LNESS laboratory.

3. Plasma asher and rapid thermal annealing (RTA)

- The plasma asher is used to remove the polymer from the sample. To do that the sample is placed inside a vacuum chamber in which a monoatomic oxygen plasma is generated. In this way the free radicals that have the role of the reactive species combines with the polymer, or as in this thesis with the graphene, generating CO_2 that is then removed from the chamber by a vacuum pump.
- The RTA is a rapid thermal annealing of the sample. It is obtained by the heating of the sample by means of a high intensity radiation. Usually the duration of the process goes from 1 to 600 seconds. In particular the machine is made by a quartz oven unit in which the wafer is loaded by a quartz isolation tube. Two lamps provide the heating of the wafer inside the oven, one above the quartz tube and the other below it.

Bibliography

[1]S.O.Kasap, Principles of electronic materials and devices, 4th edition, McGraw-Hill Education, 2017.

[2]Antonio Di Bartolomeo, Graphene Schottky diodes: An experimental review of the rectifying graphene/semiconductor heterojunction, Physics reports, Volume 606, 8 January 2016, Pages 1-58.

[3]Electronic properties and quantum transport in Graphene-based nanostructures Dubois, SM., Zanolli, Z., Declerck, X. et al. Eur. Phys. J. B (2009) 72: 1. https://doi.org/10.1140/epjb/e2009-00327-8.

[4]A.H. Castro Neto, F. Guinea, N.M.R. Peres, K.S. Novoselov, and A.K. Geim The electronic properties of graphene, Rev. Mod. Phys. 81 (2009) 109-162.

[5]K.I. Bolotin, K.J. Sikes, J. Hone, H.L. Stormer, P. Kim, Temperature-Dependent Transport in Suspended Graphene, Phys. Rev. Lett. 101 (2008) 096802 (4pp).

[6]A.K.M. Newaz, Y.S. Puzyrev, B. Wang, S.T. Pantelides, K.I. Bolotin, Probing charge scattering mechanisms in suspended graphene by varying its dielectric environment, Nature Communications 3 (2012) 734.

[7]A. Venugopal, J. Chan, X. Li, C. W. Magnuson, W.P. Kirk, L. Colombo, R.S. Ruoff, E.M. Vogel, Effective mobility of single-layer graphene transistors as a function of channel dimensions, J. Appl. Phys. 109 (2011) 104511 (pp 5).

[8]L.A. Falkovsky Optical properties of graphene, Journal of Physics: Conference Series 129 (2008) 012004 (pp 7).

[9]Li, X.M., Zhu, Hongwei, The graphene–semiconductor Schottky junction , Phys.Today vol.69, 2016/09/01, doi: 10.1063/PT.3.3298.

[10]S. Tongay, T. Schumann, A.F. Hebard, Graphite based Schottky diodes formed on Si, GaAs, 4 H-SiC substrate, Appl. Phys. Lett. 95 (2009) 222103.

[11]Y. An, A. Behnam, E. Pop, A. Ural, Metal-semiconductor-metal photodetectors based on graphene/p-type silicon Schottky junctions, Appl. Phys. Lett. 102 (2013) 013110.

[12]Gang Niu, Giovanni Capellini, Grzegorz Lupina, Tore Niermann, Marco Salvalaglio, Anna Marzegalli, Markus Andreas Schubert, Peter Zaumseil, Hans-Michael Krause, Oliver Skibitzki, Michael Lehmann, Francesco Montalenti, Ya-Hong Xie, and Thomas Schroeder, Photodetection in Hybrid Single-Layer Graphene/Fully Coherent Germanium Island Nanostructures Selectively Grown on Silicon Nanotip Patterns, ACS Applied Materials & Interfaces **2016** 8 *(3)*, 2017-2026, DOI: 10.1021/acsami.5b10336.

[13]Shi Qiang Li, Amit Solanki, Jacopo Frigerio, Daniel Chrastina, Giovanni Isella, Changxi Zheng, Arman Ahnood, Kumaravelu Ganesan, and Kenneth B., Vertical Ge–Si Nanowires with Suspended Graphene Top Contacts as Dynamically Tunable Multispectral Photodetectors, Crozier ACS Photonics 2019 6 (3), 735-742 DOI: 10.1021/acsphotonics.8b01646

[14]C. V. Falub, H. von Kanel, F. Isa, R. Bergamaschini, A. Marzegalli, D. Chrastina, G. Isella, E. Muller, P. Niedermann, and L. Miglio.

Scaling Hetero-Epitaxy from Layers to Three-Dimensional Crystals. Science , 335(6074):1330–1334, 2012.

[15]Jacques I.Pankive, Optical processes in semiconductors, Dover, 1975.